

CHAPTER

7

The sediment routing system

Earth felt the wound, and Nature from her seat Sighing through all her works gave signs of woe That all was lost.

(JOHN MILTON, *PARADISE LOST* (1667))

SUMMARY

The sediment routing system is the integrated geomorphic system involving sediment liberation, transport, and deposition. Understanding this complex system in terms of its physical laws and response times is important for the evaluation of sediment supply to sedimentary basins, which controls the stratigraphic architecture of the basin-fill (Chapter 8).

Pristine rock exposed at the Earth's surface is subject to physical and chemical weathering. The regolith is the weathering mantle between pristine bedrock and the land surface. The thickness of the regolith is principally dependent on two rate effects: the rate of bedrock weathering, and the rate of removal by erosion, both of which are strongly controlled by climatic and topographic factors. Regolith production rates are believed to decay exponentially with depth, and estimates from cosmogenic radionuclide analysis indicate bedrock to regolith conversion rates of $10\text{--}50 \times 10^{-6} \text{ myr}^{-1}$.

The flux connecting land and ocean reservoirs in the hydrological cycle is termed run-off. It varies strongly depending on climatic variables. Run-off transports sediment from source regions to sinks. The sediment yield is the total sediment discharge of the catchment, measured at the river mouth, divided by its area, and therefore has the units of a mass flux. Sediment yields can be estimated from the infilling rate of artificial reservoirs and lakes, and by calculating the volume of dated sediment in offshore depocenters. Global patterns of sediment yield show an arc of very high yields from Japan to the mouth of the Indus, where high rates of precipitation combined with young tectonic topography are found. There have been many attempts to identify the principal controls on sediment yield, such as rate of pre-

cipitation, or topographic variables such as elevation and relief. Recent analyses point to different controls in high relief, tectonically active regions *versus* low relief, tectonically inactive regions.

Chemical weathering also results in the release of ions in solution, which are transported away as a dissolved load, measured as total dissolved solids (TDS). The type of bedrock undergoing chemical weathering, and the climatic and topographic influences on precipitation, weathering, and evaporation, are crucial to understanding the amount and constituents of the dissolved load. The global average of solute load is roughly one-fifth of the global average of suspended particulate load, but the ratio varies strongly. Rivers in mountainous terrains have high particulate sediment yields, whereas lowland rivers tend to have high levels of dissolved load.

Measurements of erosion rates can also be made using a range of methods including thermochronologic techniques such as apatite fission track analysis and U-Th/He dating, and from analysis of cosmogenic radionuclides. Comparison of erosion rate estimates derived from different techniques with varying temporal resolution provides valuable insights into the functioning of the erosional system. In general, longer time scale and larger spatial scale "geological" estimates of erosion are strongly smoothed relative to the characteristics of individual erosive "geomorphic" events.

The engine for the sediment routing system is the coupled process systems of hillslopes and rivers, which degrade the topography produced by tectonics. In mountainous regions, rivers commonly cut down like cheese wires through regionally uplifting bedrock, and are supplied with the products of hillslope mass wasting. Landsliding dominates on hillslopes above a critical gradient.

Hillslope evolution can be modeled as a diffusive process, by making use of the sediment continuity equation and the assumption that the hillslope mass flux is proportional to the local topographic gradient. Hillslope profiles are therefore parabolic, but where channel incision rates are high, landsliding produces linear hillslope profiles. The spacing of transverse drainages and their maximum relief scales on the tectonic uplift rate of rock, as seen in the Southern Alps of New Zealand.

The products of hillslope erosion are transported away by rivers. The rate of incision of bedrock rivers can be estimated by different methods, but the most common approach is to approximate the incision rate by an area-slope or discharge-slope product. The increasing discharge downstream and the reducing slope downstream combine to produce maximum incision rates at a certain distance from the drainage divide. Deep incision by rivers causes an erosional unloading that may result in an isostatic uplift of mountain peaks. Such a process is likely to be responsible for the very high topography at the edges of major plateau regions such as Tibet.

Far-field sediment transport takes place in alluvial systems. The physics of long range sediment transport is complex. However, a common approach is to combine approximations and assumptions of uniform flow down an inclined plane, a flow resistance equation, conservation of discharge of water and the sediment continuity equation to derive a diffusive rule for alluvial systems. The transport coefficient can be regarded as varying smoothly in the downstream direction, or being constant for gravel ($0.01 \text{ km}^2 \text{ yr}^{-1}$) and sand ($0.1 \text{ km}^2 \text{ yr}^{-1}$), which successfully simulates the commonly observed “gravel front” in alluvial rivers. A two-diffusion numerical model shows the sensitivity of alluvial system behavior and alluvial stratigraphy to variations in forcing mechanisms such as sediment flux, subsidence rate, and gravel fraction. Tectonic-geomorphic systems have characteristic response times that may be long compared to the periodicity of any forcing. This implies that such systems may be frequently out of equilibrium with ambient forcing conditions, and that stratigraphic signals in basins are strongly smoothed by the buffering effect of large river systems.

A range of numerical landscape evolution models are currently available targeted at the understanding of coupled tectonic-geomorphic systems at a range of scales from extensional fault blocks and thrust-related folds to entire orogenic belts or passive margin megascarpments. Landscape evolution models are successful at simulating realistic landscapes, but are more important

as a tool in investigating complex system behavior. A particularly fruitful line of research concerns the evolution of river drainage over evolving extensional fault arrays and contractional fold-thrust belts.

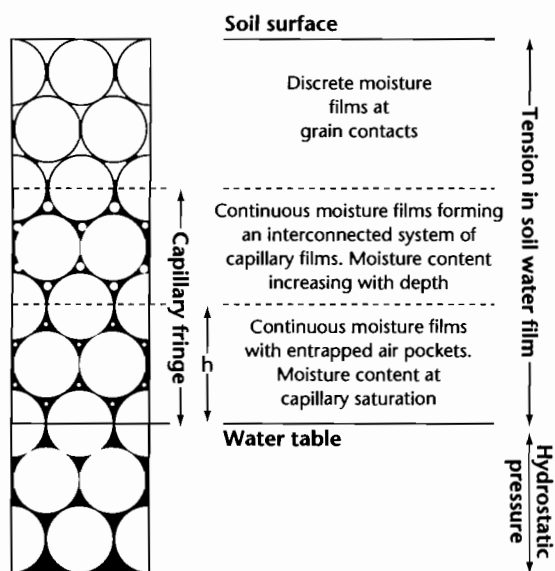
7.1 INTRODUCTION

The sedimentary character of basins is determined by the balance between tectonic subsidence causing long term accommodation and sediment influx. Sedimentary basins should not therefore be regarded as passive receptacles, but as dynamic entities occupied by complex physical and biologic process systems. This chapter concerns the geomorphologic and biogeochemical process systems or subsystems operating in the hinterlands of sedimentary basins. These hinterlands are source areas for particulate and dissolved river-borne mass fluxes. It is clearly important to be able to predict the long term mass flux from hinterlands to sedimentary basins and also the response time of the hinterland to changes in forcing variables such as climate and tectonics. Much research at present is targeted at understanding the coupling between erosion and tectonics at the medium to large spatial scales appropriate to sedimentary basins.

The structure of this chapter is to initially consider the global patterns of weathering and erosion. The transfer of mass from hillslope to basin will then be looked at in the context of sediment routing systems. We will be particularly concerned with how sediment routing systems function as physical systems. The development of landscape as a complex response to on-going tectonics is investigated in the contexts of tilted extensional fault blocks and thrust-related anticlines in fold-thrust belts. Having investigated the controls on and sensitivity of sediment transport systems, the reader is in a better position to appreciate the full set of parameters controlling stratigraphic architectures and variability of depositional style in the basin-fill in Chapter 8.

7.2 WEATHERING

Weathering is the decay and disintegration of rock *in situ* at the Earth's surface. A weathering mantle forms between pristine bedrock and the land surface, known as *regolith*. Water moves up and down in the regolith by capillary action and gravity respectively (Fig. 7.1). The presence of an enveloping and reactive moisture film is



h = height of equivalent rise in a capillary tube

Fig. 7.1 The zones of moisture in the regolith, showing the extent of the capillary fringe (after Carson 1969).

critical to the weathering of bedrock and regolithic materials.

The processes and products of weathering have been treated exhaustively elsewhere. A useful treatment is found in the excellent text by Summerfield (1991) and is considered in a geochemical context in Andrews et al. (1995). An overview is given in Allen (1997). Weathering is conventionally divided into mechanical and chemical categories. Mechanical weathering involves: (i) processes causing a volumetric change in the rock mass, including exfoliation, insolation, and hydration weathering, and (ii) processes causing a volumetric change through the introduction of material, commonly water, but also salts, into pores, void spaces, and fissures in the rock mass, such as freeze-thaw processes and salt weathering. Although these processes of mechanical weathering may be locally dominant, chemical weathering is of greater global importance.

7.2.1 Chemical weathering processes

Chemical weathering involves the chemical breakdown of bedrock and the formation of new mineral products. The main chemical weathering processes are:

- 1 *Solution* involves the action of water as a solvent. The tendency of a mineral to dissolve in water is expressed by its *equilibrium solubility*. This is affected by the temperature and pH of the local environment. As an example, quartz (SiO_2) has a low solubility below a pH of 10, but is highly soluble in very alkaline waters above this value. Alumina (Al_2O_3) is only soluble in conditions seldom found in nature, below a pH of 4 and above a pH of 9. As a result, alumina accumulates as a residue during weathering, whereas silica may be slowly leached. Calcium carbonate (CaCO_3), in contrast, has a steadily decreasing solubility in alkaline waters. However, the low solubility of CaCO_3 in pure water is rarely applicable in the natural environment because dissolved CO_2 in water causes CaCO_3 to be replaced by calcium bicarbonate $\text{Ca}(\text{HCO}_3)_2$, which is highly soluble (see "Acid hydrolysis").
- 2 *Oxidation and reduction* involves the gain or loss of charge by the addition (reduction) or loss (oxidation) of negatively charged electrons. The oxygen dissolved in water is the most common oxidizing agent. Oxidation results in the formation of oxides and hydroxides, as in the oxidation of sulfides such as iron pyrite (FeS_2) under anaerobic conditions to produce sulfuric acid and iron hydroxide. The oxidation of organic matter in soils by bacteria produces CO_2 and therefore generates acidity. The acidity is then used in the hydrolysis of minerals (see "Acid hydrolysis"). The tendency for oxidation and reduction to take place is indicated by the *redox potential* (Eh), measured in millivolts.
- 3 *Hydration* involves the absorption of water into the crystal lattice, making it more porous and therefore more susceptible to weathering. A common example is the transformation of the iron oxide hematite to the hydrated iron hydroxide limonite.
- 4 *Acid hydrolysis* is the reaction of a mineral with acidic weathering agents, where the acidity is mainly derived from the dissociation of atmospheric CO_2 in rainwater and soil zones by respiration of plant roots and bacterial decomposition of plants, producing in both cases carbonic acid (H_2CO_3). Hydrolysis involves the replacement of metal cations in the crystal lattice such as K^+ , Na^+ , Ca^{2+} , and Mg^{2+} by the hydrogen or hydroxyl ions of water. The released cations combine with further hydroxyl ions, commonly to form *clay minerals*. Examples are the hydrolysis of albite (plagioclase feldspar $\text{NaAlSi}_3\text{O}_8$) to *kaolinite* ($\text{Al}_2\text{Si}_2\text{O}_5(\text{OH})_4$), and the hydrolysis of orthoclase feldspar (KAlSi_3O_8) to *illite* ($\text{K}_2\text{Al}_4(\text{Si}_6\text{Al}_2\text{O}_{20})(\text{OH})_4$). Such reactions in general produce a clay mineral residue plus the release of

silica, metal cations, and bicarbonate ions in solution. Acid hydrolysis involving CO_2 is commonly termed *carbonation*. Carbonation dominates the weathering of limestones.

7.2.2 The regolith

The mineralogic composition of the regolith is determined not just by the type and intensity of chemical weathering processes, but also by the parent bedrock. There are considerable differences in the way basalts and granites weather under the same climatic regime. Clay minerals are particularly diagnostic of both weathering processes and parent material. A primary factor is the extent of leaching, which strips minerals of their metal cations and eventually of their silicon and iron, leading to a stable aluminum-rich residue (gibbsite).

A large throughput of water is necessary for advanced stages of leaching, leading to regoliths dominated by gibbsite, kaolinite, and aluminum oxides and hydroxides. This is only accomplished in regions of high precipitation rates such as the equatorial and humid tropical regions (Fig. 7.2). The process is commonly termed *laterization*. Where leaching is less intense, the cations released by the breakdown of bedrock promote the formation of cation-bearing clay minerals such as those of the illite and smectite groups. These zones of moderate leaching typify the temperate zones of Asia, Europe, and North America. In arid and semi-arid climates, there are very low rates of chemical weathering and little accumulation of weathering products except for carbonates and salts as hard crusts and concretions.

The clay mineral assemblage is not only a function of climate, but also of position within the regolith profile. This is because the flux of water generally decreases with depth in the regolith, caused by a downward reduction in permeability. Residual minerals such as kaolinite and gibbsite are consequently found at the top of weathering profiles, whereas smectite and illite may be found at deeper levels in the same regolith where leaching is less intense.

The thickness of the regolith depends on the trade-off of two rate effects:

- 1 Rate of bedrock weathering, which is strongly controlled by climatic factors;
- 2 rate of removal by denudation, which is controlled by climatic, tectonic, and topographic factors (§7.3).

Regoliths can only attain great thicknesses (over 100 m) in localities with humid, warm climates, and

subdued topography. Even in these situations, regolith growth is self-limiting since the development of a thick weathered mantle decreases permeability and reduces the throughput of water to the weathering front in contact with pristine bedrock. Although studies suggest that weathering rates are higher under some finite thickness of regolith than on bare bedrock, the rate of regolith production is commonly assumed to decay exponentially with regolith thickness (Anderson and Humphrey 1990):

$$E_w = k_w \exp(-m_w R) \quad (7.1)$$

where E_w is the rate of descent of the bedrock–regolith weathering front, k_w is a coefficient representing the pristine bedrock weathering rate (units of L T^{-1}), m_w is a weathering rate decay constant (equal to $1/R_0$, where R_0 is the depth at which the weathering rate reduces to $1/e$ of its surface value k_w), and R is the regolith thickness. Under such circumstances of low bedrock weathering under thick regoliths, weathering activity may be restricted to intense leaching of the soil zone. The length scale R_0 is likely to be of the order of 1 m.

Regolith production rates are difficult to measure directly. New techniques in *cosmogenic radionuclide dating*, however, now allow more reliable estimates to be made. Cosmogenic radionuclides (such as ^{10}Be and ^{26}Al) are produced *in situ* by cosmic radiation, at a rate P_0 dependent on latitude and altitude (Lal 1991; Bierman 1994). The principle is that the production rate in a bare piece of bedrock P decays exponentially with depth below the surface y (Fig. 7.3), so that

$$P = P_0 \exp(-y/y^*) \quad (7.2)$$

where y^* is a rate constant equal to 0.5–0.7 m for most common lithologies (that is, the production rate decays downwards to P_0/e in a distance y^*). The rate of change of concentration with time is then the production rate $P(t)$ minus the rate of decay λN

$$\frac{\partial N}{\partial t} = P(t) - \lambda N \quad (7.3)$$

where N is the concentration of cosmogenic radionuclides per unit volume of rock and λ is a decay constant analogous to a half-life.

Regolith shields the underlying bedrock from bombardment by cosmic rays, reducing radionuclide production rates at the regolith–bedrock interface. If the thickness of regolith H at a site is constant over time

(losses at the surface balancing production of regolith from bedrock), the rock to regolith conversion rate is

$$E = \frac{\{P_0 \exp(-H/y^*)\} y^*}{N} \quad (7.4)$$

where E is the bedrock lowering rate. Application of this technique, for example in the Wind River Range of USA

(Small et al. 1999), showed that bedrock to regolith production rates were of the order of just $10 \times 10^{-6} \text{ myr}^{-1}$. This is much lower than typical erosion rates in tectonically active areas (§7.4).

In steep mountains with humid climates, although the rate of regolith production is high, it is removed by hillslope erosion. The combination of high regolith production caused by climatic factors and high topography

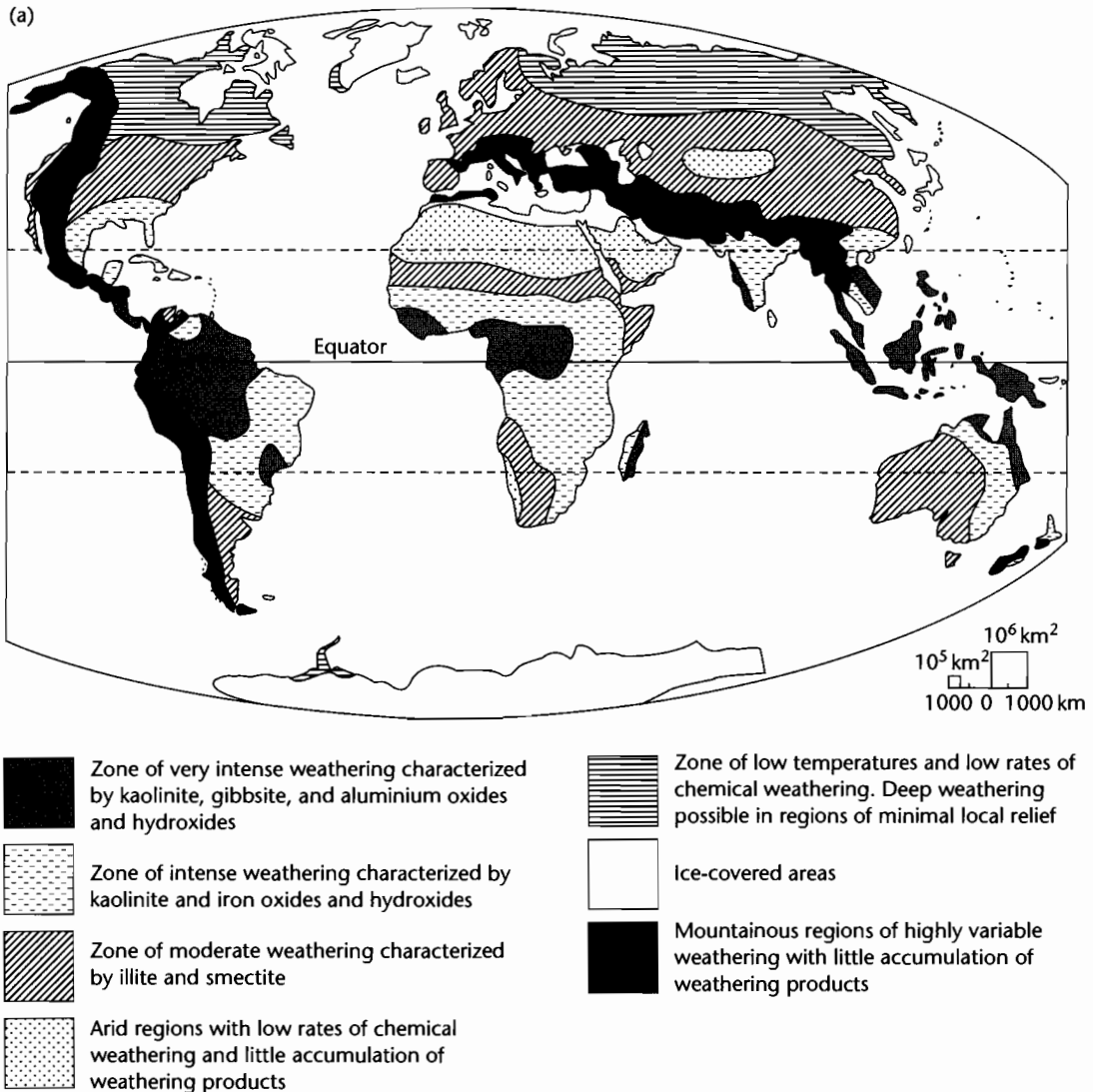


Fig. 7.2 The global pattern of weathering, modified from Strakhov (1967). (a) Map of major weathering zones, (b) latitudinal zonation showing regolith thickness and type.

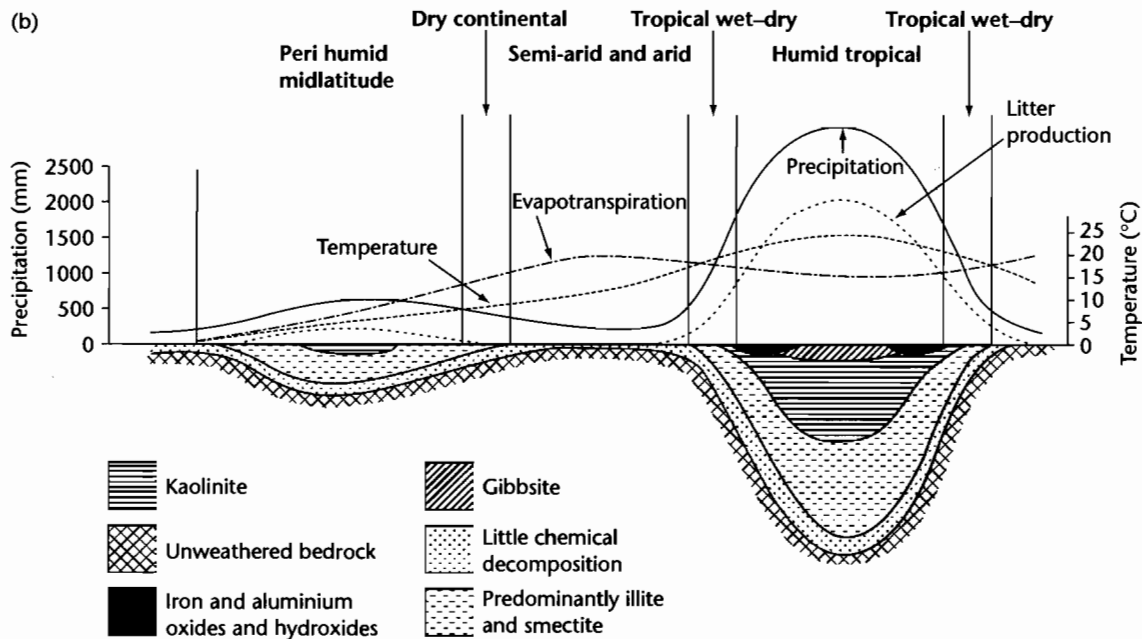


Fig. 7.2 *Continued*

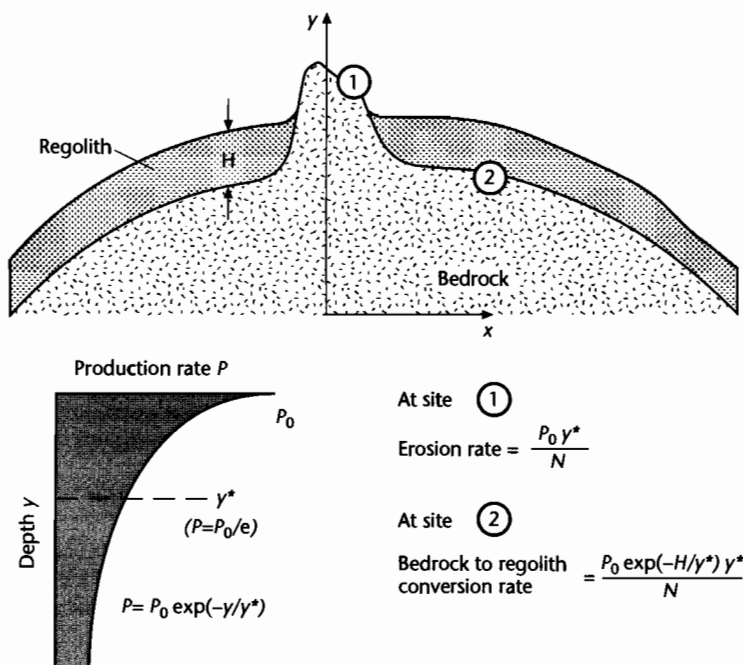


Fig. 7.3 Calculation of bedrock erosion and regolith production rates using cosmogenic radionuclides (after Burbank and Anderson 2001). At site 1, bedrock erosion rate depends on the production rate of the radionuclide at the sample site P_0 , the depth rate constant y^* , and the concentration of radionuclides per unit volume of rock N . At site 2, bedrock is converted to regolith at a rate that is also affected by the thickness of the regolith H (see equations 7.2–7.4).

caused by tectonic factors produces optimum conditions for the erosional sediment efflux of the landscape.

In summary, there are a number of factors controlling the rate of chemical weathering:

- **Organic activity** in soils generates soil acidity (CO_2) through decomposition, aids the retention of water through the build-up of organic matter and biologic activity promotes permeability;
- **climate** controls weathering reactions through the effect on chemical kinetics of temperature, imparting a latitudinal gross pattern of chemical weathering rates (Fig. 7.2). Rainfall controls vegetation type, biologic activity in the soil and the activity of water as a solvent;
- **kinetics of mineral reactions**; chemical weathering requires pore waters to be undersaturated with respect to the mineral being weathered. Once saturation is achieved, an increase in the flow rate will not cause further reaction. Whereas the chemical weathering of evaporites is determined by the rate of removal of the saturated solution by flushing, in relatively insoluble minerals such as silicates the rate of chemical weathering is determined by the kinetics by which ions are detached from crystal surfaces;
- **bedrock composition** controls the stability of the mineral components to weathering through their degree of polymerization, as illustrated by the *Goldich series*. Monomer silicates like olivine are most easily weathered, and framework silicates such as quartz are most resistant;
- **topography** influences the rate of removal of regolith by erosion, which invigorates chemical weathering by subjecting new, fresh bedrock to weathering. Topography also controls drainage and therefore rates of flushing. Flow rates on mountainous slopes are high, but flat, poorly drained slopes have very low flow rates;
- **time** is required for chemical changes to take place. Weathering profiles are seldom in equilibrium with surface conditions.

Since chemical weathering depends on temperature (as well as the other factors noted above), it is commonly assumed that chemical weathering rates for silicates are approximated by an Arrhenius-type relationship (White and Blum 1995):

$$\tau_T = A \exp(-E_a/RT) \quad (7.5)$$

where τ_T is the rate of chemical weathering (as a function of temperature), A is a prefactor that varies with the chemical species being weathered, E_a is the activation energy (in kJ mol^{-1}), R is the Universal gas constant, and

T is absolute temperature (K). In gross terms this temperature dependence is shown by the latitudinal global pattern of weathering shown in Figure 7.2.

7.3 TERRESTRIAL SEDIMENT AND SOLUTE YIELDS

7.3.1 An introduction to continental run-off

The bulk of particulate and dissolved solids is transported from the continents by running water. This flux connecting land and ocean reservoirs of the hydrologic cycle is known as *run-off*. It can be viewed most simply in the context of a simple box model for the global water cycle. There is a net gain in the fluxes between the land and atmosphere (precipitation exceeds evaporation over the land areas), which is compensated by a run-off flux from the land to the ocean reservoirs. Although the quantity of water in the continental part of the hydrologic cycle is small compared to the ocean reservoir, the flux of water from land to ocean is considerable.

Rain is not simply channeled through rivers to the ocean. The surface water balance contains run-off as one component

$$P = E + T + \Delta S + \Delta G + R \quad (7.6)$$

where P is precipitation, E is evaporation, T is transpiration, ΔS is the change in storage of water in the soil, ΔG is the change in storage of water as groundwater, and R is run-off – the overland flow across the land surface as rills and gullies, streams, and rivers.

The relative importance of these parameters depends on climatic, topographic, and geological setting, with important regional variations. The ratio of streamflow measured from a river and the precipitation falling over the drainage basin is called the *run-off coefficient* C_r . The run-off coefficient varies strongly, principally according to climatic setting and the extent of human interference through irrigation and damming. The drainage basins listed in Table 7.1 provide some representative examples. The humid tropical (Amazon, Orinoco) and cold climate (Lena) drainage basins have high run-off coefficients compared to arid region catchments (Nile, Murray).

Major variations in run-off can be predicted by comparing global maps of precipitation versus evaporation:

- Mean annual precipitation is highest in the tropics where humid air rises because of convectional insta-

Table 7.1 Run-off of a selection of the world's major rivers.

River	Catchment area (km ²)	Annual precipitation (mm yr ⁻¹)	Discharge at river mouth (m ³ s ⁻¹)	Run-off coefficient C _r
Amazon	6,150,000	1490	200,000	0.69
Nile	2,715,000	832	317	0.004
Lena (Russia)	2,430,000	355	16,200	0.59
Orinoco	945,000	1300	34,900	0.9
Murray (Australia)	910,000	582	698	0.04
Seine (France)	78,600	711	685	0.39

bility, in mountainous regions because of orographic cooling, and between 35° and 60°N and S associated with atmospheric instability causing storms;

- mean annual evaporation is highest where there is a heat source, a plentiful source of water, and low moisture contents in the air; these conditions are best satisfied in the subtropical oceans. Evaporation rates over dry continental areas are commonly much lower because of the scarcity of liquid water.

Precipitation exceeds evaporation in equatorial and high temperate to polar latitudes, whereas there is a net deficit in the subtropics. More than half of the global run-off occurs in South America, where it is concentrated in the equatorial regions. The Amazon River alone contributes 15% of the total annual global run-off.

7.3.2 Sediment yield

The erosion of the terrestrial surface results in a flux of sediment from source regions to depositional sinks. The closed system involving an erosional sector, a transport sector and a depositional sector is known as a *sediment routing system* (Allen 1997). The fluxes of sediment through the process subsystems of erosion, transport, and deposition are dependent not only on the processes operating within the subsystems, but also on the linking processes between the subsystems. This is particularly true of the transfer of sediment from the erosional zone to the transport zone. The functioning of sediment routing systems will be considered in §7.5. Here, we initially concentrate on a more descriptive approach to the global patterns of sediment production from erosional areas and its delivery to sedimentary basins.

The denudation of a drainage basin with area A_d results in a discharge of sediment and solute to the ocean

or to lakes. If D is the total discharge of sediment and solutes at the exit of the drainage basin, and there is no change in the storage of sediment within the drainage basin over time, the long term average denudation of the drainage basin per unit area (Fig. 7.4) is simply

$$\frac{\partial h}{\partial t} = \frac{(1 - \phi) D}{\rho A_d} \quad (7.7)$$

where h is the elevation, ϕ is the porosity of rocks of density ρ in the catchment undergoing weathering and erosion, and the discharge D is measured as mass per unit time (kg yr⁻¹). Measurement of both the particulate and solute loads in rivers is required to calculate the total average denudation of the catchment. If D_i denotes the particulate sediment discharge, equation (7.7) can be rewritten as

$$Y = \frac{D_i}{A_d} \quad (7.8)$$

where Y is termed the *sediment yield*, with units of kg m⁻² yr⁻¹. Sediment yield therefore has the units of a *mass flux*. For example, the Amazon River at its mouth has a solid load of 1150 Mt yr⁻¹ and a solute load of 223 Mt yr⁻¹ (1 mega ton is 10⁹ kg). The drainage area is 6,150,000 km². The sediment yield is therefore 187 t km⁻² yr⁻¹, whereas the total average denudation rate is 223 t km⁻² yr⁻¹. For a rock density of 2700 kg m⁻³ and an average porosity of 5%, the catchment-wide average denudation rate (equation 7.7) is 79 mm kyr⁻¹. Although this figure is very low, it should be remembered that certain parts of the Amazon drainage basin in the Andes are experiencing very rapid denudation while large parts of the floodplain are undergoing no denudation at all.

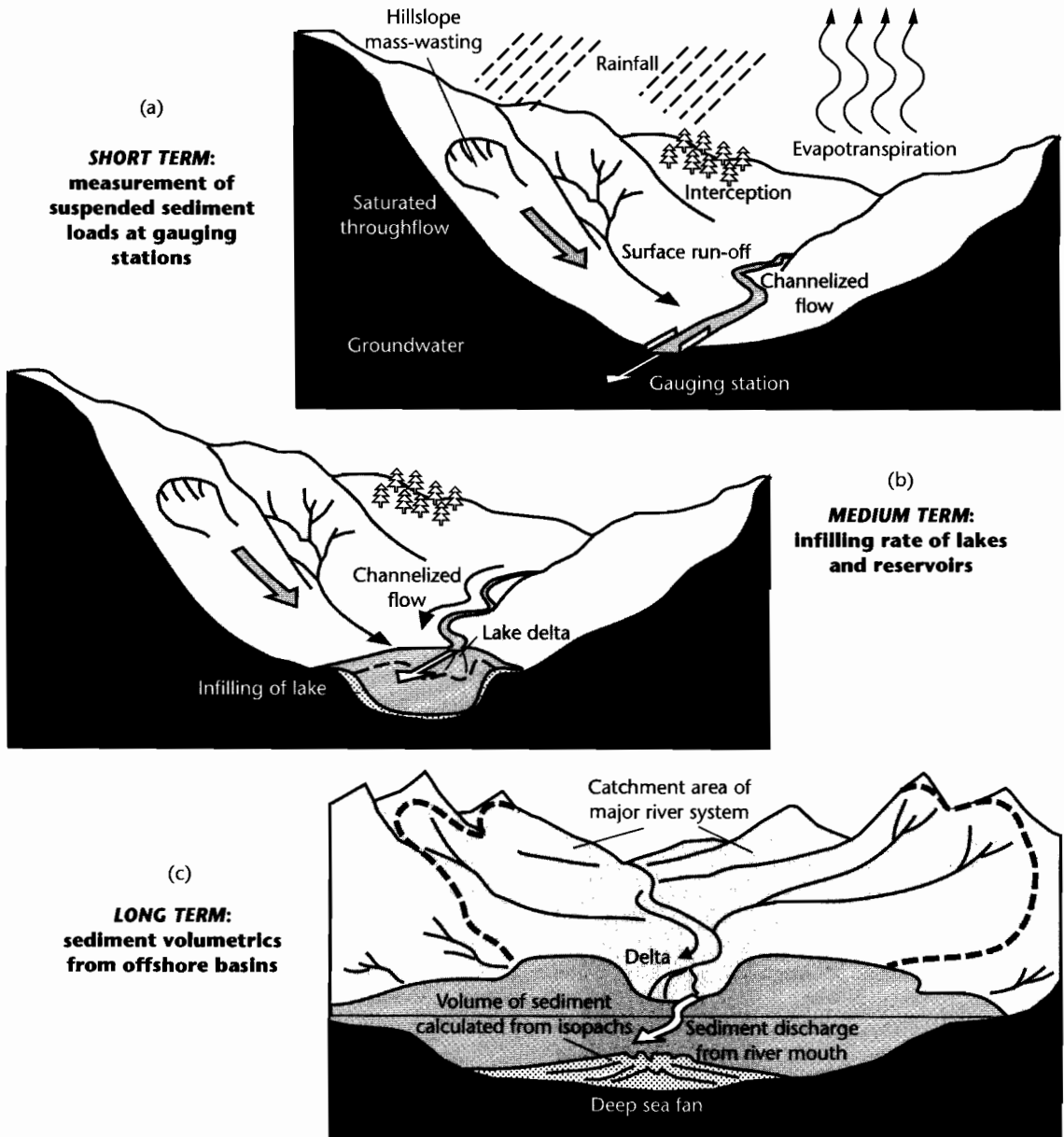


Fig. 7.4 Methods of estimating sediment yield. In (a), the short-term sediment yield is the discharge of sediment in kg yr^{-1} measured at a gauging station divided by the contributing catchment area. In (b), the medium-term sediment yield is the infill rate of a lake basin or artificial reservoir divided by the contributing catchment area. In (c), the long term sediment yield is the solid sediment volume derived from sediment isopachs of dated intervals of the stratigraphy divided by the paleocatchment area.

There are two strategies for evaluating catchment-averaged sediment yields and mechanical denudation rates based on the sediment exported from the catchment: use of the rate of filling of artificial reservoirs and natural lakes, and calculation of the volume of sediment accumulated in sedimentary basins.

Einsele and Hinderer (1997) studied the filling of artificial reservoirs and lakes in order to estimate sediment yields in the contributing drainage basins. In open lakes and reservoirs the solutes are assumed to be flushed through, but the particulate load is mostly trapped, allowing a sediment budget to be calculated. For example, the Tarbela reservoir on the Indus River near Islamabad is an artificial lake extending 80 km upstream from the dam, covering an area of 625 km². It has a mean depth of 22 m, giving it an initial storage capacity of 13.9 km³. The drainage area in the predominantly semi-arid north-western Himalaya is 171,000 km². The rate of filling of the reservoir (about 2% per year) indicates that the average sediment yield is 1170 t km⁻² yr⁻¹. The present-day mechanical denudation rate for the Indus catchment is therefore just over 400 mm kyr⁻¹.

The High Aswan reservoir in southern Egypt is 500 km long and covers an area of 5000 km², with a storage capacity of about 130 km³. The drainage area feeding the reservoir is 1.839 × 10⁶ km². After 25 years of operation the reservoir had collected 2800 to 3300 × 10⁶ t of sediment. Three other reservoirs in SE Sudan upstream of the Aswan High Dam have accumulated about the same amount of sediment as the main Aswan reservoir, giving a total of about 6000 × 10⁶ t. The annual accumulation rate is therefore 240 × 10⁶ t yr⁻¹. The sediment yield for the upper and middle reaches of the Nile River system is c. 130 t km⁻² yr⁻¹, and the mechanical denudation rate (using $\rho = 2750 \text{ kg m}^{-3}$ and $\lambda = 0.05$) is 45 mm kyr⁻¹, an order of magnitude less than in the Himalayan Indus catchment.

An allied strategy is to estimate the volume of sediment in the depositional zone of the sediment routing system using isopachs and cross-sections derived from borehole and seismic reflection data. The average solid phase accumulation rate for Asian sedimentary basins since the beginning of the Tertiary has been calculated after correction of stratigraphic thicknesses for the effects of compaction (Métivier et al. 1999) (Fig. 7.5). The Bengal basin, for example, contains a vast amount of Upper Tertiary sediments (locally <21 km in thickness) deposited primarily from southwestward-prograding deltas feeding a large deep sea cone. The Bengal Basin has accumulated 12 × 10⁶ km³ solid volume during the

Tertiary, with a rate of 0.45 × 10⁶ km³ Myr⁻¹ over the last 2 Myr. The Bengal basin has received sediment from the Ganges, Brahmaputra and the rivers of the eastern platform of India (Mahanadi, Krishna, and Godavari), which have a total drainage area of c. 2.266 × 10⁶ km². The average mechanical denudation rate for these Indian Subcontinent catchments during the Quaternary is about 200 mm kyr⁻¹, with an average sediment yield of 546 t km⁻² yr⁻¹ (using $\rho = 2750 \text{ kg m}^{-3}$). The Ganges, Brahmaputra, Mahanadi, Krishna, and Godavari rivers have a combined river mouth discharge of 0.49 × 10⁶ km³ Myr⁻¹. This is in excellent agreement with the estimate derived from the volume of preserved stratigraphy, and indicates that present day discharges in large, buffered systems may be closely representative of longer term (geological) rates (Einsele et al. 1996; Métivier and Gaudemer 1999; Métivier et al. 1999).

7.3.3 Global patterns of sediment yield

The total amount of sediment discharged to the ocean is estimated to be c. 20 × 10⁹ t yr⁻¹ (Milliman and Syvitski 1992; Walling and Webb 1996). Since the land surface of the Earth is 1.48 × 10⁸ km², the globally averaged sediment yield is 135 t km⁻² yr⁻¹, but there is enormous variability around this globally averaged figure (Fig. 7.6). Some of the highest sediment yields come from rugged oceanic islands such as Java, New Guinea, Taiwan, and New Zealand (Table 7.2). Even higher values (>50,000 t km⁻² yr⁻¹) come from Chinese rivers draining the easily erodible loess region. At the other extreme, there are some very large river systems with sediment yields of less than 1 t km⁻² yr⁻¹, such as the Yenesei and Dneiper Basins of the former Soviet Union.

The main features to come out of the numerous published sediment yield maps (e.g., Milliman and Meade 1983; Walling and Webb 1983; Lvovich et al. 1991) (Fig. 7.6) are that sediment yields are highest in an arc around the Pacific and Indian Ocean margins from Pakistan to Japan. This area is characterized by Cenozoic mountain building, steep topography, and generally high annual rainfalls. Low sediment yields typify desert regions and the cold, formerly glaciated, low-relief regions of Eurasia and Canada. The key question is what controls this wide variability in sediment yield. If the answer to this question were known, it would assist the understanding of the likely mass fluxes to sedimentary basins in the geological past. Sediment yield models commonly use the sediment loads of rivers as an index of sediment yield (Milliman

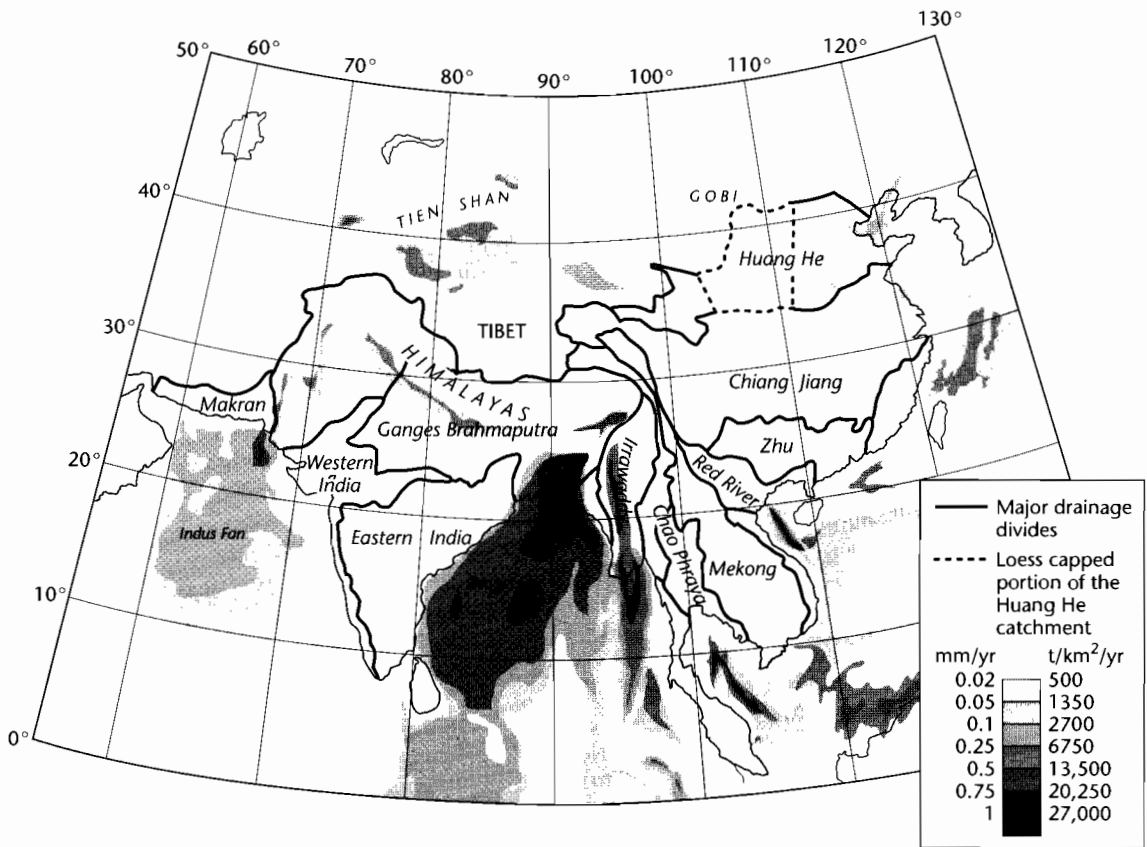


Fig. 7.5 Sediment mass accumulated in basins of south and southeastern Asia during the last 2 Myr, digitized from a large number of sources by Métiévier et al. (1999). The sediment was delivered to the ocean by the river systems of Asia. Reproduced courtesy of Blackwell Publishing Ltd.

and Meade 1983; Summerfield and Hulton 1994; Hovius 1997; Hay 1998). These sediment load data are strongly biased towards measurements made at the mouths of the world's major rivers, although Milliman and Syvitski (1992) have emphasized the influence of small mountainous streams on the global sediment budget. The sediment loads at river mouths are affected by the extent to which sediment is stored in river floodplains. The extent of storage is likely to increase in larger drainage basins with substantial depositional and transportational components of the sediment routing system. This storage

effect explains the well-established inverse relationship between drainage basin area and sediment yield (Fig. 7.7) (Milliman and Meade 1983; Milliman and Syvitski 1992). This inverse relationship has, however, been questioned as a fundamental property of natural drainage systems, and has been attributed at least in part to human impact (Walling and Webb 1996).

There are a large number of problems with the use of data on sediment loads measured at river mouths (Milliman and Meade 1983). The most obvious is that the effects of human activities, such as land use, dam con-

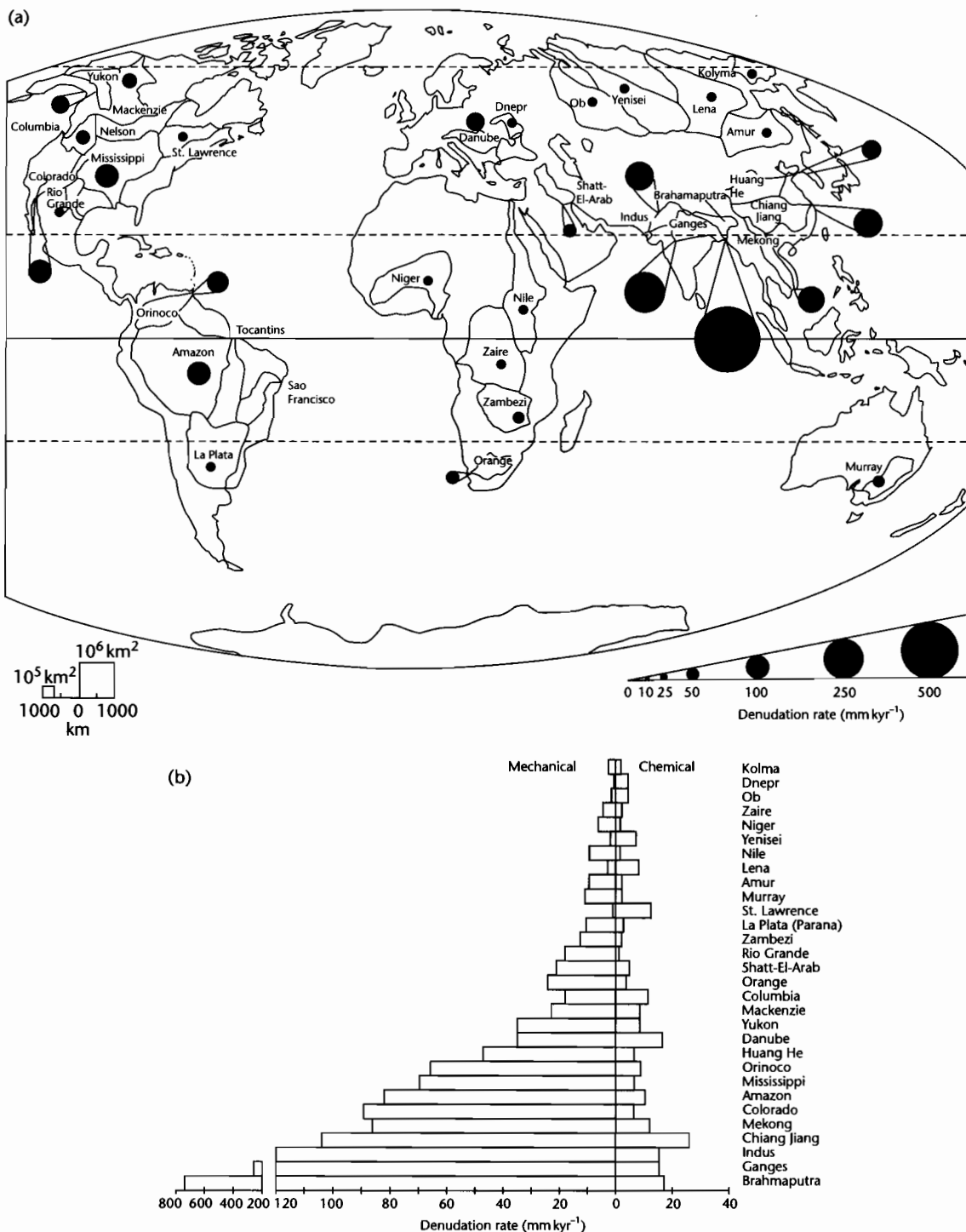


Fig. 7.6 (a) Estimated total denudation rates for major externally drained basins. Size of black circles is proportional to denudation rate; (b) Histogram comparing mechanical and chemical denudation rates for the world's major externally drained basins. After Summerfield and Hulton (1994). Reproduced courtesy of American Geophysical Union.

Table 7.2 Sediment and solute yields of the world's major rivers (after Summerfield and Hulton 1994, and sources cited therein).

River basin	Area 10 ⁶ km ²	Sediment yield t km ⁻² yr ⁻¹ (equivalent mechanical denudation rate, mm kyr ⁻¹)	Solute yield t km ⁻² yr ⁻¹ (equivalent chemical denudation rate, mm kyr ⁻¹)	Chemical denudation as % of total
Amazon	5.98	221 (82)	29 (11)	11.6
Amur	2.04	28 (10)	6 (2)	17.6
Brahmaputra	0.64	1808 (670)	49 (18)	2.6
Chiang Jiang	1.73	281 (104)	72 (27)	20.4
Colorado	0.70	239 (89)	19 (7)	7.4
Columbia	0.67	48 (18)	32 (12)	40.0
Danube	0.79	94 (35)	45 (17)	32.4
Dnepr	0.54	2 (1)	12 (4)	85.7
Ganges	0.98	694 (257)	42 (16)	5.7
Huang He	0.79	127 (47)	18 (7)	12.4
Indus	0.93	323 (120)	42 (16)	11.5
Kolyma	0.65	9 (3)	4 (1)	30.8
La Plata (Parana)	2.86	30 (11)	9 (3)	23.1
Lena	2.45	7 (3)	22 (8)	75.9
Mackenzie	1.77	62 (23)	23 (9)	27.1
Mekong	0.76	232 (86)	36 (13)	13.4
Mississippi	3.20	189 (70)	20 (7)	9.6
Murray	1.14	30 (11)	6 (2)	9.7
Nelson	1.24	—	16 (6)	—
Niger	2.16	19 (7)	4 (1)	17.4
Nile	3.63	28 (10)	3 (1)	9.7
Ob	2.98	6 (2)	11 (4)	64.7
Orange	0.89	65 (24)	11 (4)	14.5
Orinoco	0.92	179 (66)	23 (9)	11.4
Rio Grande	0.63	48 (18)	4 (1)	7.7
Sao Francisco	0.62	11 (4)	—	—
Shatt-El-Arab	0.89	56 (21)	14 (5)	20.0
St Lawrence	1.05	2 (1)	34 (13)	94.4
Tocantins	0.76	—	—	—
Yenisei	2.55	5 (2)	18 (7)	78.3
Yukon	0.84	94 (35)	23 (9)	19.7
Zaire	3.63	14 (5)	6 (2)	30.0
Zambezi	1.41	34 (13)	6 (2)	15.0

struction and irrigation schemes, must be accounted for. In addition, measured sediment loads are invariably suspended load only, with the bedload contribution ignored. This is unlikely to be a problem in the downstream reaches of large rivers, but may introduce a significant error in short, steep, mountainous streams. Finally, the suspended load sediment data have been collected using different methods over protracted periods of time and are difficult to compare.

Glaciated terrains appear to have a different and more complex relation between sediment yield and catchment size than river basins (Hallet et al. 1996). Sediment delivery from the upland part of glaciated catchments may be particularly high when pluvial conditions promote the rapid evacuation of loose morainic material from a previously glaciated region. Some currently glaciated basins, such as the steep and wet catchments of Alaska and the Southern Alps of New

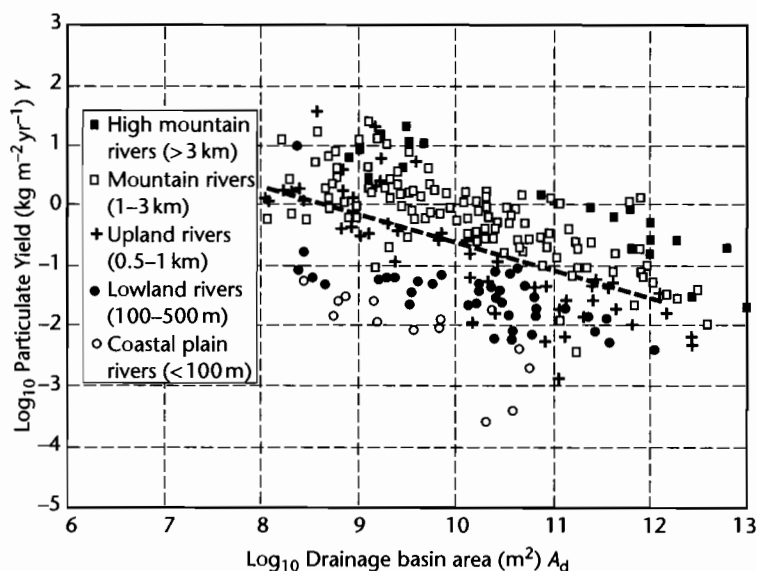


Fig. 7.7 Plot of drainage basin area versus particulate sediment yield for the elevation classes of rivers of Milliman and Syvitski (1992). The regression for all of the river data has the form $Y = \exp(9.18 - 0.46 \ln A_d)$. After Hay (1998). Reproduced courtesy of Elsevier.

Zealand, also have very high yields, in excess of most nonglaciated settings.

7.3.4 Controls on sediment yield

Numerous attempts have been made to correlate sediment yield with topographic and climatic factors. The resulting relationships invariably work reasonably well at restricted spatial scales, or in certain prescribed geomorphic settings, but involve a large amount of scatter at the global scale.

7.3.4.1 Rates of precipitation

A number of authors have investigated the link between sediment yield and mean annual precipitation, rainfall variability, and specific run-off (water discharge per square kilometer of drainage basin, in mm yr^{-1}). Any relationship between precipitation and run-off variables and sediment yield must be strongly mediated by the effects of vegetation (Leeder et al. 1998). There is some consensus that sediment yield reaches a maximum in semi-arid areas where vegetation cover is sparse, with a second maximum where mean annual precipitation exceeds 1000 mm. Since most hillslope processes are sensitive to

the intensity of rainfall, however, the rainfall peakedness (ratio of average monthly precipitation and maximum monthly precipitation) may be more important in governing sediment yield (Fournier 1960). The effects of vegetation cover can be seen where catchments have been disturbed by human activities. Sediment yields from cleared, agricultural land is higher (by factors of up to 100) than from forested catchments. On steep, mountainous slopes, the magnification of sediment yield may be even higher.

7.3.4.2 Topographic effects

A number of workers have linked erosion rate to a variety of topographic parameters such as mean or maximum elevation, large-scale or local relief, slope and drainage basin area. Various correlations have been claimed for a range of different datasets. For example, these comprise the sediment discharges of 280 rivers, including small mountainous streams (Milliman and Syvitski 1992), a dataset of 285 drainage basins of varying size and climatic zone (Allen 1997, Hovius 1998), a subset of the world's largest 29 rivers (Summerfield and Hulton 1994), a compilation of sediment yields in central Europe (humid temperate climate) up to 1981 based on reservoir and lake studies (Schröder and Theune 1984), and a

selection of mid-latitude drainage basins (Ahnert 1970; Pazzaglia and Brandon 1996).

The bewildering range of correlations with topographic and climatic parameters claimed by different authors suggests that erosion rate data cannot be compressed onto one simple plot. A multivariate analysis of sediment yield data reveals that a combination of environmental and topographic factors only explains about half of the variance in global sediment yield data (Hovius 1997, 1998). However, when plotted against a proxy for tectonic uplift rate (Fig. 7.8), tectonically inactive and tectonically active settings are clearly discriminated. For example, tectonically inactive cratonic settings are characterized by very low sediment yields of $<100 \text{ t km}^{-2} \text{ yr}^{-1}$, whereas currently or recently tectonically active contractional mountain belts have sediment yields of $100\text{--}10000 \text{ t km}^{-2} \text{ yr}^{-1}$. Pinet and Souriau (1988) similarly noted different relationships for young, tectonically active orogens and old, tectonically inactive landscapes. This suggests that physical insights based on the different sets

of processes dominating in low relief and high relief areas must be included in the analysis.

Montgomery and Brandon (2002) suggested a non-linear regional-scale relation between erosion and mean slope derived from a digital elevation model (DEM):

$$E = E_0 + \frac{KS}{[1 - (S/S_c)^2]} \quad (7.9)$$

where E is the erosion rate, E_0 is a background erosion rate due to chemical weathering ($\approx 0.01 \text{ mm yr}^{-1}$ based on the mean chemical denudation rate for the world's 35 largest drainage basins, Summerfield 1991), S is the mean slope, S_c is a limiting hillslope gradient for landsliding, and K is a rate constant. Here, mean slope is derived from the range of values within a 10 km diameter analysis window around points spaced every 2 km, using a 10 m-resolution DEM. In the Olympic Mountains of Washington, USA, $E_0 = 0.016\text{--}0.059 \text{ mm yr}^{-1}$, $K = 0.6 \text{ mm}$

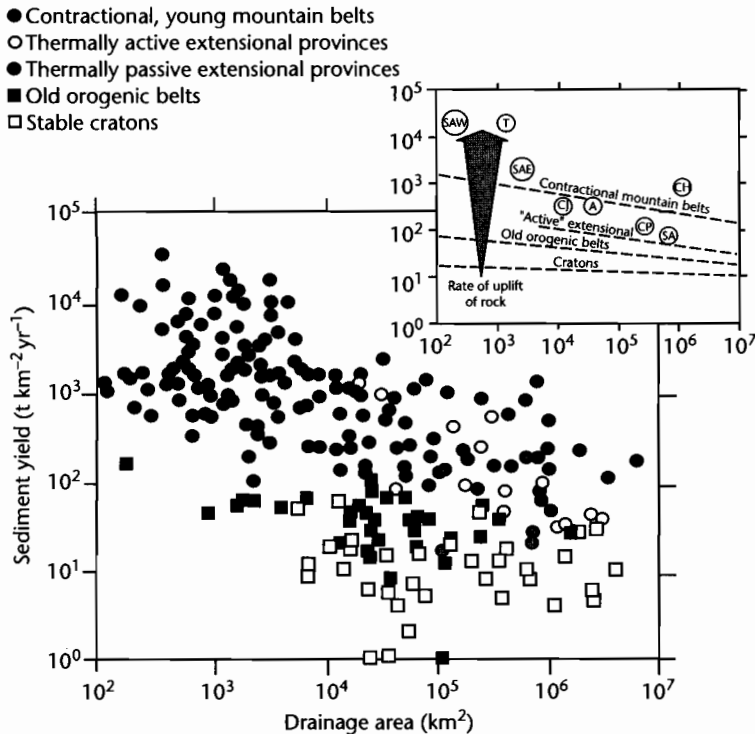


Fig. 7.8 Plot of sediment yield versus drainage basin area for five categories of tectonic setting, derived from Hovius (1995) using the sediment yield data of Milliman and Syvitski (1992). SAW, Southern Alps New Zealand western flank; SAE, Southern Alps New Zealand eastern flank; T, Taiwan; CJ, Central Japan; A, Alps; CP, Colorado Plateau; SA, Southern Africa; CH, Central Himalaya.

yr^{-1} , and $S_c = 40^\circ$. Equation (7.9) can be expressed in terms of a mean local relief, derived from the same 10-m-resolution DEM with a 10-km-diameter analysis window, giving

$$E = E_0 + \frac{KR_z}{[1 - (R_z/R_c)^2]} \quad (7.10)$$

where R_z is the mean local relief, and R_c is the limiting local relief. Data from low relief, tectonically inactive areas show a linear relation between erosion and mean local relief, as previously suggested by Ahnert (1970). However, this linear relation does not hold for high relief, tectonically active areas. In such cases, equation (7.10) gives a good fit with $E_0 = 0.01 \text{ mm yr}^{-1}$, $R_c = 1500 \text{ m}$, and $K = 2.5 \times 10^{-4} \text{ mm yr}^{-1}$ (Fig. 7.9). The mean local relief R_z

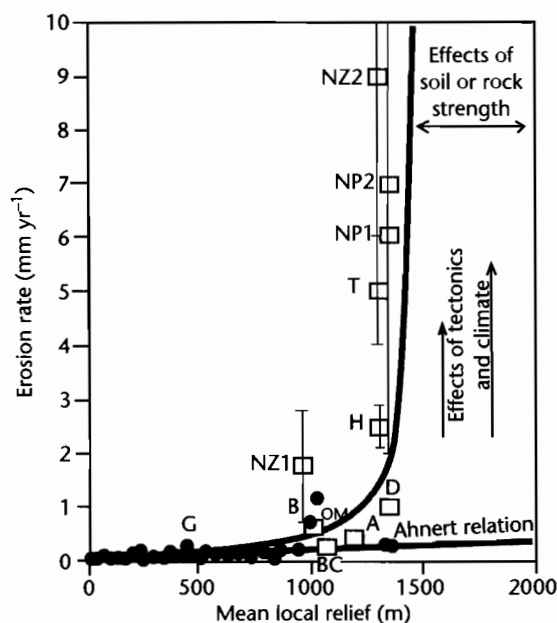


Fig. 7.9 Plot of erosion rate versus mean local relief using data compiled from Ahnert (1970), Summerfield and Hulton (1994) and Pazzaglia and Brandon (1996). Solid line is model fit using equation (7.10) with $E_0 = 0.01 \text{ mm yr}^{-1}$, $R_c = 1500 \text{ m}$, and $K = 2.5 \times 10^{-4} \text{ mm yr}^{-1}$. Squares are from tectonically active regions; NZ1 and NZ2, Southern Alps of New Zealand; H, central Himalaya; NP1 and NP2, the Himalayan portion of the Indus River Basin; BC, British Columbia Coast Range; OM, Olympic Mountains; D, Denali portion of the Alaska Range; A, European Alps. Ganges (G) and Brahmaputra (B) also shown for reference. After Montgomery and Brandon (2002). Reproduced courtesy of Elsevier.

appears to reach a maximum of $c. 1500 \text{ m}$ ($R_c = 1500 \text{ m}$), and is very rarely $>2000 \text{ m}$, suggesting that rock strength may control the maximum relief attainable in a mountain belt.

There are therefore essentially two different sorts of landscape in terms of erosion rate. In *low relief landscapes*, such as low-lying shield areas and alluvial floodplains, thick regoliths may develop. The rate of removal of regolith is determined mainly by the erosivity of the transport processes, rather than by the availability of loose, easily transportable material. This may also be the case in regions of extreme aridity where streamflow processes are negligible. In these *transport-limited* circumstances, parameters such as mean annual rainfall and specific run-off may offer the best correlation with sediment yield. Where the removal of loose material by streams is efficient, the rate of removal of sediment may, however, be limited by the rate at which loose material is supplied by hillslope weathering. These circumstances are therefore *weathering-limited*, and hillslope erosion processes determine the erosion rate, which depends linearly on mean slope or local relief. These conditions may be typical of low relief, mid-latitude, temperate zone landscapes. In *high relief landscapes*, however, physical transport processes of hillslope erosion by landsliding and channelized flow are almost always capable of removing regolith above a critical rate of rock uplift. Erosion rates then stabilize at a certain mean local relief determined by rock and soil strength. It is estimated that rock uplift rates of 1 mm yr^{-1} are required to sustain combined potential chemical and physical erosion in mountainous areas (Koons 1995). In high relief landscapes therefore, the key process is the landsliding of critically steep hillslopes and efficient removal of debris by streams.

7.3.5 Transport of dissolved loads

Chemical weathering results in the release of ions in solution. Precipitation must infiltrate to deep levels in the regolith in order to promote chemical breakdown and the flushing of solutes into the groundwater system. This process of infiltration and flushing depends on climate and topography. In semi-arid regions, water is drawn to the surface during dry periods, leading to reprecipitation of solutes, and chemical weathering is retarded. On steep slopes, water runs off hillslopes quickly and does not spend long periods in contact with bedrock and regolith. In low-lying, gently sloping areas, the regolith is poorly

drained, so flushing rates are low. Chemical fluxes are highest on gentle upland slopes, where both infiltration and flushing are moderately high. Although particulate sediment yields are far higher than solute yields in mountainous areas, solute yields are relatively higher in lowland regions.

The groundwater system delivers solutes to rivers. The solute discharge of rivers may be modified by nondegradational inputs such as precipitation, wind-blown dust, salt aerosols (particularly close to the ocean), mineralization of organic matter, plant metabolism, and human pollution. Outputs include those of evaporation and losses to groundwater and soils. Consequently, the dissolved loads of rivers cannot be simply or directly linked to rates of chemical denudation.

The chemistry of water in the hydrologic cycle strongly reflects the reactions taking place with soil, with plants and with decomposing organic matter, through dilution or concentration caused by additions of precipitation and losses by evaporation, and particularly through the weathering of rock. Waters from calcareous catchments contain high amounts of *total dissolved solids* (TDS), particularly Ca^{2+} and HCO_3^- , but small particulate loads. Waters draining varied igneous, metamorphic, and sedimentary rock types have a varied chemical composition and higher TDS.

It is customary to plot river and lake water on a graph with axes of TDS (mg l^{-1}) and the cationic ratio (Fig. 7.10)

$$\frac{\text{Na}^+}{\text{Na}^+ + \text{Ca}^{2+}}$$

or the anionic ratio

$$\frac{\text{Cl}^-}{\text{Cl}^- + \text{HCO}_3^-}$$

Waters are consequently classified in terms of the source of the solute load (Gibbs 1970):

- 1 Dominated by *atmospheric precipitation*, with low salt concentrations because of dilution ($20\text{--}30\text{ mg l}^{-1}$), and a chemistry dominated by Na^{2+} , so the cationic ratio is nearly 1. This class of water characterizes rivers draining areas of low relief with well-weathered bedrock and plentiful rainfall, such as the tropical rivers of Africa and South America.
- 2 Dominated by *weathering reactions* in rock and soil, with higher TDS and a wide spread of cationic ratio depending on the reactions involved. There is a low

ratio in limestone terrains where waters are dominated by calcium bicarbonate. In the Amazon Basin, 85% of the solute load is derived from a relatively small area of intense chemical weathering in the Andes, whereas in the lowland part of the catchment the control is by precipitation.

- 3 Dominated by *evaporation* and subsequent precipitation, with high salt concentrations ($\text{TDS } 1000\text{--}2000\text{ mg l}^{-1}$), reflecting the precipitation of CaCO_3 and the relative concentration of Na^+ and Cl^- through evaporative losses. This is common in the rivers of hot and arid climates such as the Jordan River of the Near East. These typical river compositions evolve to the composition of sea water.

The chemistry of river input to the ocean therefore varies from continent to continent and from region to region in response to variations in the control of precipitation, weathering and evaporation superimposed on the signature provided by bedrock type (see below). Rivers in arid Kazakhstan have solute concentrations of $6000\text{--}7000\text{ mg l}^{-1}$, compared to 10 mg l^{-1} for rivers in the humid Amazon Basin, where solutes are diluted by large amounts of run-off.

The measurement of the solute concentration or "salinity" of a water sample is conventionally in units of mg l^{-1} . That is, the solutes are measured as a concentration. Consequently, the transport rate of solutes is the product of the water discharge ($\text{m}^3\text{ yr}^{-1}$) and the solute concentration expressed as TDS (mg l^{-1}). The solute discharge from the world's rivers, and the solute flux from river catchments, reflect the competing effects of concentration and run-off.

7.3.6 Effects of bedrock weathering on solutes

Study of unpolluted catchments composed on one bedrock lithology illuminates, after correction for atmospheric salts, the typical solute loads of rivers draining known rock types (Meybeck 1987) (Fig. 7.11). The solute loads of rivers draining large multilithologic catchments (such as the Amazon; Stallard and Edmond 1983), or even the entire land surface of the Earth (Holland 1981), can therefore be estimated with knowledge of the percentage of each rock type comprising the region being investigated. The calculated global value for solute discharge to the ocean can then be compared with the measured average composition of rivers (Livingstone 1963; Meybeck 1979). More than 80% of the total dis-

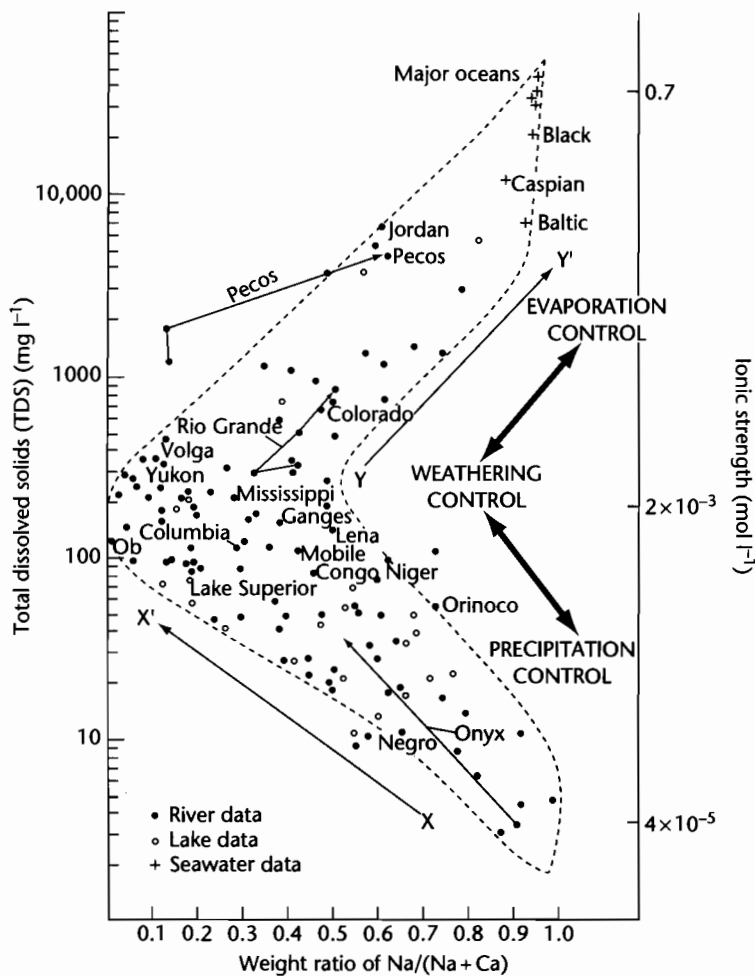


Fig. 7.10 Gibbs's (1970) scheme for global water chemistry, wherein the total dissolved solids (TDS) and ionic strength of surface waters are plotted against the cationic weight ratio of $\text{Na}/(\text{Na} + \text{Ca})$. The arrows connecting data points show the geochemical evolution of river waters from source downstream. Rivers plotting along the trend from X–X', such as the McKenzie (Arctic Canada) and Ganges (India), occur in regions with highly active weathering processes. Rivers falling along the trend from Y–Y', such as the Jordan (Middle East), Rio Grande and Colorado (arid southwestern North America) occur in areas experiencing high amounts of evaporation, and evolve towards the composition of sea water.

solved load of the world's rivers is made of four ions: HCO_3^- , SO_4^{2-} , Ca^{2+} , and SiO_2 .

The geographic origin of river-borne material has an important impact on the total dissolved solids and suspended loads, expressed as percentages of the total input to the oceans (Table 7.3). The dissolved and suspended loads from cold, temperate, tropical, and arid regions shows that the tropical zone dominates the world's run-

off. It is therefore the major source of silica and organic carbon. The dissolved silica reflects the high rates of chemical weathering in tropical regions. Despite occupying 17% of the Earth's surface, the arid regions contribute a minute amount of run-off. However, the total ions, though small, are 4 to 5 times the volume of run-off, indicating higher ionic concentrations in arid region rivers. Cold regions, despite occupying 23% of the

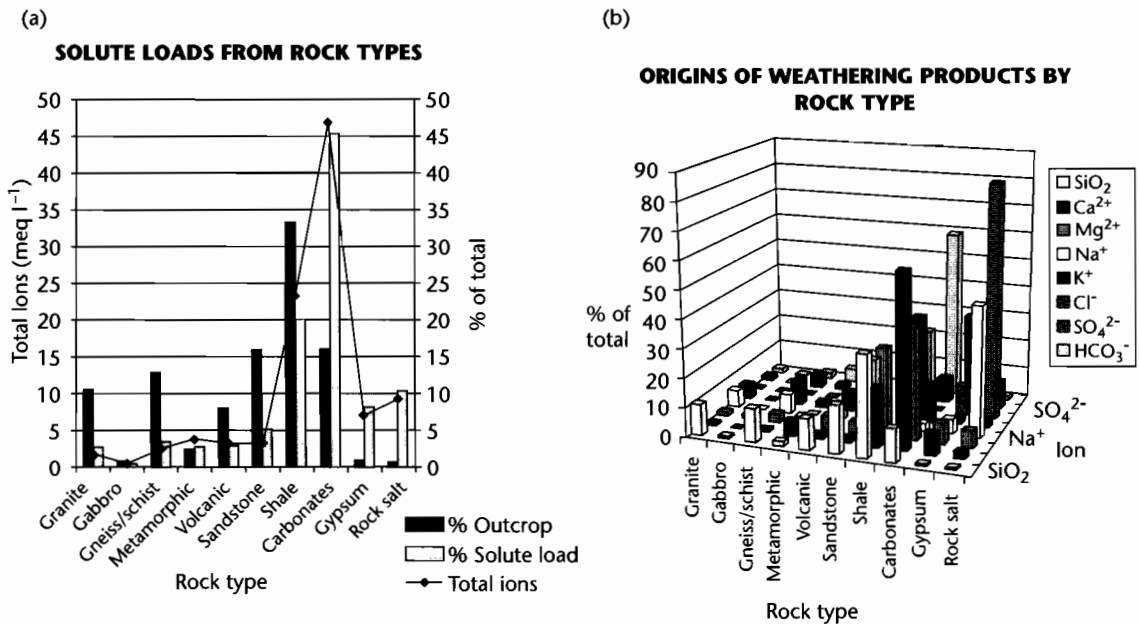


Fig. 7.11 (a) Solute loads (meq l⁻¹) from a range of common rock types compared to their outcrop area; (b) Distribution of eight major ions according to rock type, expressed as a percentage of the total solute load. Data from Meybeck (1987).

Table 7.3 Dissolved and suspended loads of rivers in different climatic regions. TOC is total organic carbon.

Geographic region	Area (%)	Run-off (%)	Dissolved SiO ₂ (%)	Ions (%)	TOC (%)	Suspended matter (%)
Cold regions	23.4	14.7	5.4	15.5	17.5	2.7
Temperate	22.4	27.5	19.9	39.9	28.5	56.5
Tropical	37.0	57.2	73.6	41.8	52.0	34.2
Arid	17.2	0.65	1.0	2.8	1.3	6.6

Earth's surface, contribute less than 3% of the suspended matter to the ocean.

7.3.7 The composition of waters draining different rock types

The surface of the Earth is covered with different rock types (Table 7.4). The weathering of these rock types produces distinct chemistries of solutes in the run-off. (Atmospheric contribution of salts must be accounted for if necessary and care must be taken to exclude all anthropogenically affected waters.) If we combine the typical water analyses of major rock types with their relative

abundance on the surface of the continents, we get a global picture of the solute delivery to the ocean from rivers (corrected for atmospheric salts). The solutes derived from different rock types is shown in Figure 7.11a.

Taking *granite* as a standard, the chemical weathering rates of the world's major rock types (Table 7.5) shows that evaporites and carbonates weather most rapidly. Volcanic and noncrystalline metamorphic rocks and shales weather at moderate rates, while granites, gneisses, gabbros, and sandstones have low rates of weathering. Chemical sediments, such as carbonates and evaporites (which have high yields of solutes), and shales (which are very extensive) therefore dominate the solute fluxes of

Table 7.4 Rock types at the Earth's surface by percentage.

Class	Rock type	Percentage (by area)
Plutonic	Granite	10.4
	Gabbro and ultrabasics	0.6
Metamorphic	Marble	0.4
	Amphibolite	1.9
	Mica-schist	1.5
	Gneiss	10.4
	Quartzite	0.8
Volcanic	Basalt	4.15
	Andesite	3.0
	Rhyolite	0.75
Sedimentary	Quartz-arenite	12.6
	Arkose (felspathic arenite)	0.8
	Greywacke (lithic, argillaceous arenite)	2.4
	Shale	33.1
	Limestone and dolomite	15.9
	Evaporite (gypsum and halite)	1.3

Table 7.5 Weathering rates of major rock types, relative to granite.

Rock type	Weathering rate
Granite	1
Gneiss/schist	1
Gabbro	1.3
Sandstones	1.3
Volcanics	1.5
Shales	2.5
Other metamorphic	5
Carbonates	12
Gypsum	40
Rock salt	80

ivers draining to the ocean. Crystalline rocks have a minor contribution to global weathering in terms of solutes.

In terms of individual elements (Fig. 7.11b), *silica* and *potassium* originate mostly by weathering of silicates. *Sodium* is derived mostly from the weathering of the salt halite (NaCl), the remainder coming from the weathering of silicates. *Magnesium* originates from both dolomites, silicates and to a lesser extent Mg-rich evaporites. *Calcium* is mainly derived from the weathering of carbonates.

Chloride is complicated by the contamination from the atmosphere, but is strongly controlled by the dissolution of halite. *Sulfate* comes from the weathering of pyrite, evaporitic sulfate, and organic sulfur compounds. *Bicarbonate* is derived from atmospheric and soil CO₂ as well as from the dissolution of carbonate rocks.

7.3.8 Relation between solute and suspended load

The global average of solute load is roughly one-fifth of the global average of suspended load, but the ratio varies from continent to continent and from drainage basin to drainage basin. A key determinant is the topographic setting of the river. In mountainous regions, the particulate sediment yield is much higher than the solute yield, whereas in lowland regions the two are roughly in balance (Fig. 7.12).

The relationship between suspended and solute load (Table 7.6) can be appreciated by completing the practical exercise available at www.erdw.ethz.ch/Allen.

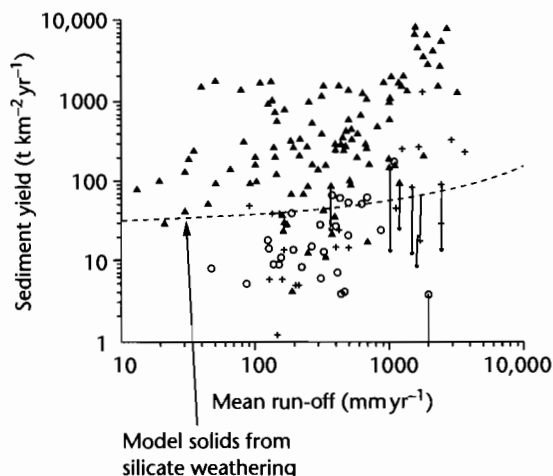


Fig. 7.12 Relation between mean run-off and sediment yield for rivers throughout the world. Open circles, coastal plain (0–100 m at headwaters) and lowland (100–500 m); crosses, upland rivers (500–1000 m); solid triangles, mountain (1–3 km) and high mountain (>3 km). Model curve is prediction for solids derived by silicate weathering (after Stallard 1995), showing that mountainous catchments provide high solid yields for a given run-off, whereas lowland rivers provide low solid yields for the same run-off.

Table 7.6 Water discharge, suspended and solute loads, and mean elevation of world's major rivers.

River	Water discharge (m^3s^{-1})	Suspended load (Mtyr^{-1})	Solute load (Mtyr^{-1})	Mean elevation (m)
Amazon	200,000	1150	223	426
Brahmaputra	19,300	520	61	2734
Columbia	7930	15	35	1329
Colville	492	520	6	469
Danube	6660	70	60	501
Dnepr	1650	2.1	11	152
Fraser	3550	20	11	1140
Ganges	11,600	524	75	890
Indus	7610	250	41	1855
Irrawaddy	13,600	260	92	758
Jana	920	3	1	703
Lena	16,200	12	88	602
Mackenzie	9830	125	64	634
Magdalena	6980	220	28	1203
Mekong	14,900	160	60	1062
Mississippi	18,400	400	125	656
Murray	698	30	9	266
Niger	6020	32	10	429
Nile	317	125	18	662
Ob	12,200	16	50	301
Orange	2890	91	12	1241
Orinoco	34,900	150	39	456
Parana	18,000	112	56	564
Po	1490	18	10	793
Rio Grande	95	30	2	1279
Shatt al Arab	1460	103	18	669
St. Lawrence	14,300	4	59	265
Xi Jiang	9510	80	132	670
Yangtze	28,500	480	226	1688
Yellow (Huang He)	1550	120	22	1885
Yenisei	17,800	13	65	749
Yukon	6180	60	34	741
Zaire	40,900	32.8	36	740
Zambezi	6980	48	15	1033

7.4 MEASUREMENTS OF EROSION RATES

7.4.1 Rock uplift, exhumation, and surface elevation change

There is considerable confusion in the literature regarding the terminology for various rates involved in tectonics and denudation (for discussion see England and Molnar 1990). A given point on the Earth's surface experiences vertical changes in its position relative to some reference datum such as the centre of the Earth caused by: (i) the

uplift of underlying crustal rocks caused by tectonic or isostatic processes, (ii) denudation or deposition at the surface of the Earth, and (iii) compaction of the underlying sediment pile. All of these factors may contribute to a surface elevation change. Neglecting compaction and deposition in upland areas, surface elevation change is normally the net result of rock uplift and denudation.

Now consider a crustal section through a mountain range with an average elevation h and a crustal thickness h_c , shown in Figure 7.13a. If we instantaneously erode this crustal section and do not thicken the crust tectonically to compensate for the loss of crust by erosion, it will

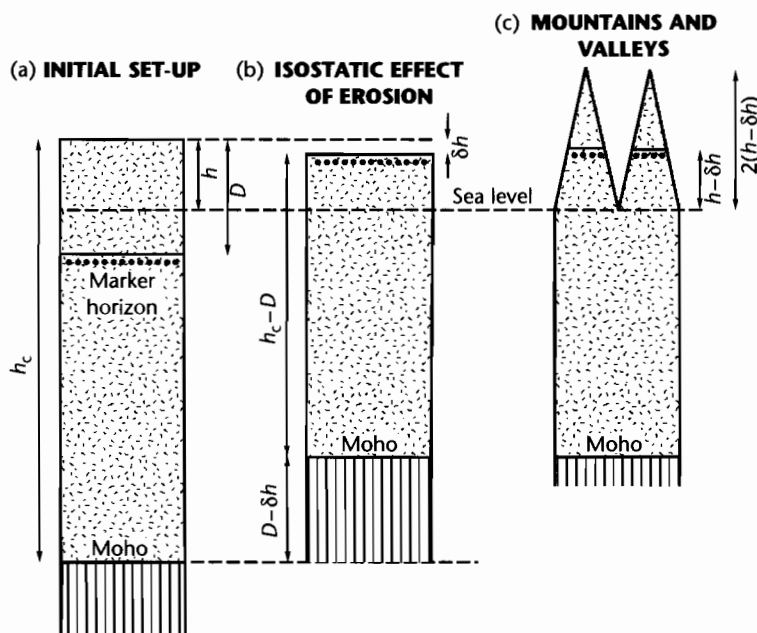


Fig. 7.13 Schematic crustal cross-sections to illustrate the possible isostatic effects of erosion on the elevation of mountain peaks and valleys, modified from Molnar and England (1990). The initial set-up in (a) shows a surface elevation of h and a marker horizon at a depth D . Erosion of amount D in (b) brings the marker horizon to the surface, resulting in a change in surface elevation Δh . In (c), rivers excavate deep valleys to sea level, which results in an uplift of the mountain peaks to an elevation $2(h - \Delta h)$, while the marker horizon remains at an elevation of $h - \Delta h$. Airy isostasy is assumed throughout.

respond isostatically to the unloading by erosion as shown in Figure 7.13b. The line with circles below it is a reference horizon in the crust. Note that it has been uplifted between (a) and (b). This is the *uplift of rock*. Note also that all of the crust above the reference horizon has been eroded between (a) and (b). This is the *exhumation* or *denudation* D . As a result of the erosion and the isostatic adjustment, there is a change in the mean elevation of the surface Δh . In this case it is a surface lowering, so the surface uplift is negative. It is essential to recognize the differences between the uplift of rock, the denudation and the surface uplift.

Now imagine that the Earth's surface is carved into mountains and valleys (as shown in Figure 7.13c). In this case the mean elevation is the same as in Figure 7.13b, but the highest mountain peaks are considerably higher than the mean elevation initially. In this sense, erosion builds mountains. The isostatic balance for the situation described above is as follows. The pressure at depth h_c in (a) is simply $\rho_c h_c g$. The pressure at the same depth after erosion (b) is $\rho_c (h_c - D)g + \rho_m (D - \Delta h)g$. Equating the two pressures and simplifying slightly, we obtain

$$\Delta h = D \frac{(\rho_m - \rho_c)}{\rho_m} \quad (7.11)$$

If $\rho_c = 2800 \text{ kg m}^{-3}$ and $\rho_m = 3300 \text{ kg m}^{-3}$, the elevation change is only 15% of the total denudation.

In Figure 7.13c valleys are carved down to sea level, and the highest peak is therefore at an elevation of $2(h - \Delta h)$. If the denudation is 4 km, the elevation change from equation (7.11) is 0.454 km. If the mountain range is initially at an elevation of 3 km, the highest peak will now be at 5 km, with deep valleys incised to sea level. Although this concept has been successfully applied to the Laramide uplifts of the Rocky Mountain region and Sierra Nevada, USA (Small and Anderson 1995, 1998) and the Himalayas (Molnar and England 1990; Burbank 1992), it probably exaggerates the uplift of the mountain peaks as an isostatic result of surface erosion.

It is also important to discriminate between local rates and regional rates of surface uplift and denudation. Whereas a local rate is measured at a point, and may be influenced by very specific tectonic and geomorphic processes such as slip on a fault or the occurrence of a

landslide, isostatic responses depend on regional rates of denudation.

7.4.2 Point-wise erosion rates from isotopic studies and other thermochronometers

There is a wide range of techniques used to estimate erosion rates at a point. Any individual technique is useful for a particular time range, using particular materials. A large number of techniques are applicable only to Quaternary materials (see Noller et al. 2000 for an excellent compilation). For example, dendrochronology (tree rings) can only be used up to about 10ka, and radiocarbon dating (^{14}C) has a useful time range of only up to 35 ka. U–Th radioisotopic dating, amino acid racemization, thermoluminescence and optically stimulated luminescence all have upper age limits of ≈ 300 ka. All of these techniques therefore are restricted to Quaternary materials and are routinely used in geomorphologic studies. The time range is significantly extended by the use of *in situ* cosmogenic radionuclides (e.g., ^{10}Be and ^{26}Al), and even further by the use of thermochronometric methods such as He diffusion during U–Th decay and apatite/zircon fission track analysis. Dating techniques making use of radiometric clocks with higher closure temperatures and longer half-lives, such as ^{87}Rb – ^{87}Sr (half-life 1.4×10^9 yr), ^{40}K – ^{40}Ar (half-life 4.89×10^9 yr), ^{235}U – ^{207}Pb (half-life 7.04×10^8 yr) and ^{147}Sm – ^{143}Nd (half-life of 1.06×10^{11} yr), provide estimates of very long term (10^6 – 10^7 Myr) erosion rates. It needs to be stressed that

the numerical values for erosion rate derived from different techniques with different temporal sensitivities cannot be directly compared (but see §7.4.4).

Since this book concerns basin analysis, we are mostly focused on the techniques providing “geological” rather than “geomorphological” rates of erosion. Use of a number of radiometric clocks with different closure temperatures (Table 7.7) allows cooling histories to be estimated. Combined with assumed or estimated geothermal gradients, these cooling histories can be used to calculate denudation rates over geological time periods. As an example, a cooling curve based on several different thermochronometers is shown for the Central Alps of Switzerland (Hurford 1986; Hurford et al. 1989) (Fig. 7.14). More recent studies across a major extensional shear zone in the Central Alps (Mancktelow and

Table 7.7 Closure temperatures of some common isotopic systems.

Mineral and dating technique	Closure temperature ($^{\circ}\text{C}$)
Hornblende (K–Ar)	525 ± 25
Monazite (U–Pb)	525 ± 25
Muscovite (Rb–Sr)	500 ± 25
Muscovite (K–Ar)	325 ± 25
Zircon (fission track)	300 ± 55
Biotite (K–Ar)	300 ± 25
Biotite (Rb–Sr)	275 ± 25
K–Felspar (K–Ar)	200 ± 25
Apatite (fission track)	110 ± 20
Apatite (U–Th/He)	70 ± 10

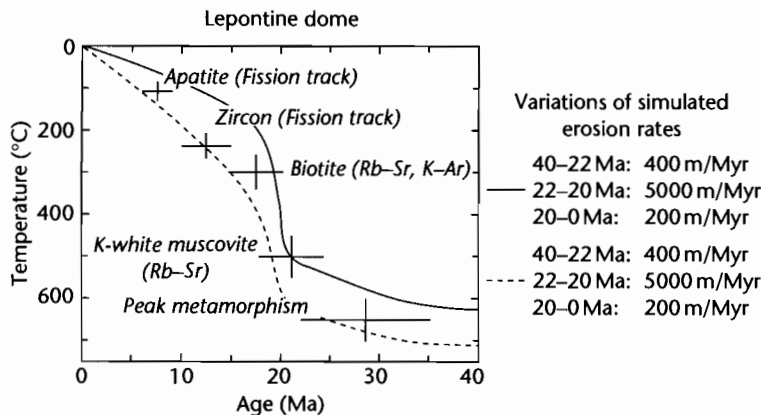


Fig. 7.14 Example of the use of a range of radiometric and thermochronometric techniques from the Lepontine dome, Central Alps, to constrain thermal (cooling) history (Schlunegger and Willett 1999). Solid and dashed lines are alternative model curves based on erosion data shown to right. Reproduced courtesy of Geological Society of London.

Grasemann 1997) show the different thermal evolution of the footwall and hangingwall blocks using multiple thermochronometers.

Conversion of a cooling history to a denudation history is not necessarily straightforward. The geothermal gradient is rarely well-constrained, though a value of $25\text{--}30^\circ\text{C km}^{-1}$ is often assumed. This geothermal gradient may be affected by changes in the basal heat flow, the internal radiogenic heat production, the advection of heat from magmas and hot fluids, and the bending of isotherms by the upward exhumation of rock towards an erosional surface of high relief. This latter effect is especially important to account for with low temperature chronometers (Fig. 7.15). Rapid erosion rates ($>5\text{ mm yr}^{-1}$) may cause very high geothermal gradients ($60\text{--}100^\circ\text{C km}^{-1}$) to exist in the exhuming rock body (Stüwe et al. 1994; Mancktelow and Grasemann 1997), and geothermal gradients may be very different between mountain peaks and valley floors (Fig. 7.15).

Further details on the use of apatite fission tracks and the (U–Th)/He method are found in §9.7.3.

7.4.3 Catchment-scale erosion rates from cosmogenic nuclides

We have previously learnt that the accumulation of cosmogenic nuclides in rocks at the Earth's surface depends on latitude, altitude, and depth below the surface. If a rock is brought closer to the surface by erosion, it experiences a greater amount of cosmic-ray bombardment. The cosmogenic nuclide abundance is therefore partly a function of the rate of erosion. If samples are taken of many detrital quartz grains derived from the catchment, it is possible to estimate a catchment-wide mean erosion rate (Brown et al. 1995; Granger et al. 1996). However, since altitude and topographic shielding affect the cosmic flux, the best results come from catchments with little (less than a few hundred meters) relief. The distribution of quartz-bearing lithologies should also be relatively uniformly distributed throughout the area of the catchment. Different erosional processes (bedrock landsliding through to soil creep) also affect cosmogenic dosages. This effect can be accounted for by considering the abundance of cosmogenic nuclides in different size classes of the total detrital sediment load. Using this technique, a 3 km^2 catchment in Puerto Rico was found to have a catchment-wide average denudation rate of 40 mm kyr^{-1} using the concentrations of ^{10}Be (Brown et al. 1995). On a

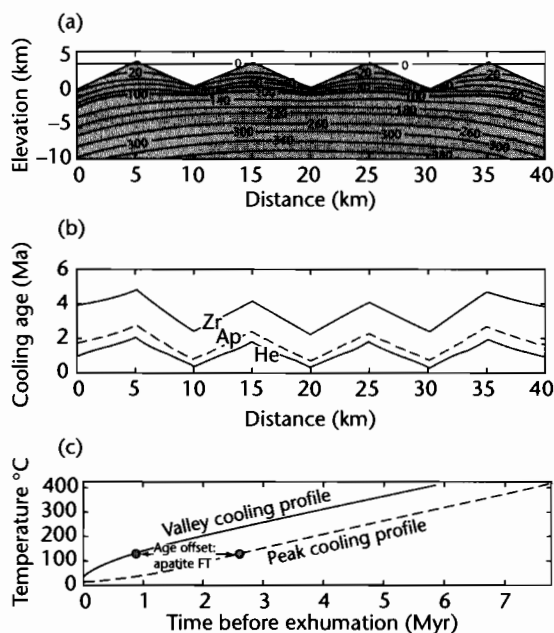


Fig. 7.15 Thermal effect of 2-D V-shaped topography (10 km wavelength, 4 km relief) on three thermochronometers with different closure/annealing temperatures; zircon fission track (Zr, 220°C), apatite fission track (Ap, 110°C) and U–Th/He (He, 60°C), from Burbank and Anderson (2001). Atmospheric lapse rate is $6.5^\circ\text{C km}^{-1}$, erosion rate is spatially uniform at 2 mm yr^{-1} , implying steady state. Note the warping of isotherms near the surface in (a), giving different geothermal gradients between the ridges and the valleys; (b) shows the expected spatial pattern of cooling ages, showing higher cooling ages for all 3 thermochronometers under the ridges; (c) shows the offset of the temperature paths of rocks exhumed in the central valley (solid) and the central peak (dashed). The apatite fission track age is offset by nearly 2 Myr. The relative effect on the cooling age is greatest for the low temperature thermochronometers, especially U–Th/He. Reproduced courtesy of Blackwell Publishing Ltd.

larger scale, Schaller et al. (2001) used ^{10}Be concentrations in quartz grains in river terraces and bedload from a number of European river basins to estimate catchment-wide denudation rates of $20\text{--}100\text{ mm kyr}^{-1}$ over the last $\approx 10^4$ years.

Erosion rates may also be calculated by measuring the isotopic signatures of river water or sediment loads, in comparison to the isotopic composition of different source lithologies in the catchment. A spatially uniform erosion of the catchment would yield isotopic signatures in water or sediment that reflected the isotopic ratio of

the parent lithology and the area (as a percentage) of the catchment occupied by this lithology. Departures from this uniform model should reflect different erosion rates in the catchment. The total denudation rate for the whole catchment can then be obtained by summing the effects of the source areas with different lithologies. The isotopic ratios of Sr and Nd in detrital clay minerals from Nepalese catchments in the Himalayas have been used in this way (Galy et al. 1996).

7.4.4 Erosion rates at different temporal and spatial scales

It is clear from the discussion above that erosion rates can be estimated at different temporal resolutions. Consequently, an erosion rate estimate derived for a very short time resolution provides very different information to the erosion rate derived for a long time resolution. For example, the rate of bedrock lowering caused by a single debris flow in an upland channel gives a local erosion rate over a time period of minutes to hours. At the other extreme, cooling histories obtained from apatite fission track studies provide estimates of erosion rates at the time scale of millions of years.

There is considerable value in compiling the variation of erosion rates derived from methods with different temporal resolution (Dadson et al. 2003). The Taiwan orogen has rock uplift rates of $5\text{--}7\text{ mm yr}^{-1}$, mean annual precipitation of 2.5 m yr^{-1} , and common strong earthquake activity, which together promote rapid rates of landsliding, debris flows, and fluvial bedrock incision (Hovius et al. 2000). Erosion rates at the decadal time scale have been calculated from the suspended sediment discharges of Taiwanese rivers at 130 gauging stations, from the rate of filling of 12 major reservoirs, and from the annual discharge of sediment into the ocean by rivers. The 30-year annual average erosion rate of Taiwan is 3.9 mm yr^{-1} using suspended load data, with significant regional differences (up to 60 mm yr^{-1} in the tectonically active SW Taiwan). Discharges of sediment into the ocean (average of 384 Mt yr^{-1} for the period 1970–2000) support the gauging station data. Erosion rates for the Holocene ($<10\text{ ka}$) have been derived from dated river terraces cut into bedrock using ^{14}C in wood or plant fragments in the alluvial veneer. Incision rates were calculated by dividing the radiocarbon age by the elevation of the bedrock terrace above the present-day river. Holocene erosion rates range from 1.5 mm yr^{-1} to 15 mm yr^{-1} , with broadly the same pattern as the rates obtained from sediment dis-

charges. Long term erosion rates derived from low temperature thermochronometry (apatite fission track) are $3.0\text{--}6.0\text{ mm yr}^{-1}$ and $1.5\text{--}2.5\text{ mm yr}^{-1}$ in the metamorphic core of the mountain belt and in the fold-thrust belt of SW Taiwan respectively. A comparison of these erosion rates suggests that despite the difference in temporal resolution, the metamorphic core of the Central Range of Taiwan has consistent values of $3\text{--}6\text{ mm yr}^{-1}$ across the temporal scales considered. However, large variations in Holocene rates are thought to reflect the more localized impact of growing tectonic structures (e.g., in the fold and thrust belt of SW Taiwan). At decadal scales, individual major earthquakes are responsible for major spatial and temporal variations in erosion rate.

We saw in §7.3.2 that erosion rates can be estimated from the sediment volumes in neighboring sedimentary basins. This enables sediment volumes of known age to be used to calculate erosion rates at the temporal resolution of the stratigraphy. The spatially and temporally variable sediment effluxes of channel-hillslope systems in individual catchments are smoothed as the sediment is transported through major fluvial systems with large storage capacities in floodplains, channel bars, and lakes. Consequently, erosion rates (sediment yields) derived from the sediment discharge at the mouths of large river systems such as the Ganges-Brahmaputra are a buffered record of the contributing inputs (Métivier et al. 1999). In addition, the sediment preserved as marine stratigraphy is a time-integrated record of the sediment discharge from the land area over the time periods resolvable from stratigraphic dating tools. In general, therefore, longer time scale and larger spatial scale “geological” estimates of erosion rate are strongly smoothed relative to the characteristics of the individually erosive geomorphic events.

7.5 THE FUNCTIONING OF SEDIMENT ROUTING SYSTEMS

The engine for the sediment routing system, termed the *clastic factory* by Leeder (1999), is the coupled process systems of hillslopes and rivers. The topography generated by tectonics is degraded through the action of this coupled system. Rivers typically become entrenched in position, cutting down like cheese wires through the regionally uplifting bedrock (Burbank et al. 1996). The intervening hillslope system provides erosional material by soil creep, overland flow, gullying, debris flows, landslides, and rockfalls. If the rate of hillslope erosion is slower than the rate of valley lowering, hillslopes steepen

and eventually become susceptible to landsliding involving bedrock. The amplitude of hillslopes is therefore set by the effect of rock strength on landsliding. The fluvial system transports away material derived from hillslope erosion through its channel networks. This evacuation of valley bottoms is particularly rapid where the stream is incising into bedrock. Evacuation may be significantly delayed where high magnitude trigger events such as earthquakes cause an instantaneous discharge from hillslopes, blocking valleys with landslide and debris flow dams. The efflux of the hillslope–bedrock channel system sets a boundary condition for far-field sediment dispersal.

In mountain ranges, landslide activity, triggered by rainstorms and coseismic shaking (Densmore and Hovius 2000), is critical to the clearing of hillslopes (Densmore et al. 1997). A number of rapidly uplifting mountain belts (Southern Alps of New Zealand, Karakorum of the western Himalayas) are believed to exhibit a steady-state topography where the tectonic rate of uplift of rock is balanced by the landslide-dominated erosional sediment efflux. In the Southern Alps of New Zealand, the flux of material due to landsliding estimated over a 60 year period ($\text{several mm yr}^{-1}$) is roughly equivalent to the sediment output of the main rivers draining the region (Hovius et al. 1997).

In the sections that follow, we present a physically based but necessarily incomplete account of the processes operating in hillslope–channel systems. These processes fashion landscapes and deliver sediment to basins. Rather than attempt a comprehensive review of

such a rapidly growing field of study, we highlight some basic modeling approaches to the evolution of hillslopes (§7.5.1), the incision of bedrock rivers (§7.5.2) and the far-field transport of sediment in alluvial rivers (§7.5.3). In doing so, the reader will appreciate the common methodologies used. We especially wish to emphasize that geomorphic systems have characteristic length scales and, importantly, characteristic response times. A fundamental concern is whether a step or cyclical change in a forcing parameter results in a system response that is short or long compared with the frequency of the forcing process. This will strongly impact on our ability to “invert” stratigraphic signals to interpret forcing mechanisms. Finally, we introduce some additional concepts in numerical landscape models as a way of integrating many of the ideas found in the preceding sections.

7.5.1 Modeling hillslopes

The evolution of hillslopes can be modeled as a diffusive process, in a manner similar to the 1-D conduction of heat (Chapter 2). Sediment diffusion models are based on two first-order assumptions: (i) the *sediment continuity equation*, which states that the spatial variation in the sediment transport rate is proportional to the vertical erosion or aggradation rate of the substrate, assuming there to be no changes in the concentration of suspended sediment (see Allen 1997, pp.180–1) (Boxed text 7.1), and (ii) that the flux is proportional to the local gradient, which is a basic notion underpinning all diffusional problems.

BOXED TEXT 7.1: The Sediment Continuity Equation

We derive the sediment continuity equation by the conservation of mass in an alluvial channel, and then apply it to the topographic evolution of hillslopes.

Consider an area of stream bed with unit width normal to the flow and length parallel to the flow of dx with a height of h above some reference datum (Fig. 7.16). The area of this piece of stream bed is therefore dx . A fluid flow with suspended sediment volume concentration C has a sediment transport rate (per unit width of stream bed) at the upstream end of the reference area (q_{s1}) and at the downstream end of the reference area (q_{s2}). We can denote the difference in the transport rate at the upstream and downstream ends of the reference area as dq_s . Any change in the

bed elevation due to either erosion or deposition must be reflected in a downstream change in the sediment transport rate as long as the sediment concentration C does not change. The amount of sediment deposited over the reference area associated with a downstream decrease in the sediment transport rate is simply the product of the difference between the upstream and downstream sediment transport rates (dq_s) and the time interval dt . This sediment produces a layer of thickness dh with a porosity λ over an area dx . Expressed mathematically

$$dh \, dx = -\frac{1}{1-\lambda} dq_s \, dt \quad (7.12)$$

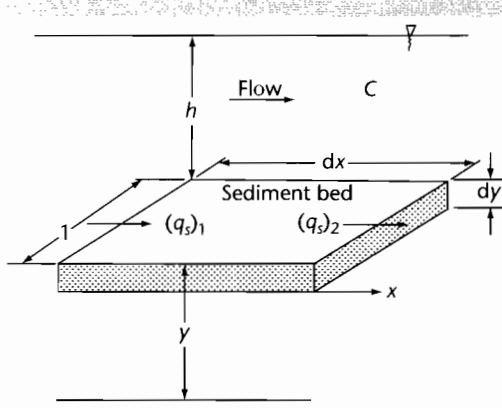


Fig. 7.16 Set-up and notation for the derivation of the sediment continuity equation. Notation explained in text.

A change in bed elevation may also result from a temporal change in the volume concentration of suspended sediment throughout the flow. For example, if the suspended sediment concentration throughout the flow is decreasing, the bed must be accreting irrespective of downstream variations in the sediment transport rate. The bed elevation change due to this effect in a flow of depth h is

$$dh \, dx = -\frac{1}{1-\lambda} (dC \, h) dx \quad (7.13)$$

The net change in bed elevation over a time interval dt is therefore

$$\frac{dh}{dt} = -\frac{1}{1-\lambda} \left(\frac{dq_s}{dx} + h \frac{dC}{dt} \right) \quad (7.14)$$

In other words, the change of bed elevation in time (erosion or deposition) is related to the downstream change of the sediment transport rate and to the change of the suspended sediment concentration in time. If the suspended sediment concentration does not vary in time, that is, $dC/dt = 0$, or if the suspended sediment concentration is zero, then the sediment continuity equation simplifies to

$$\frac{dh}{dt} = -\frac{1}{1-\lambda} \frac{dq_s}{dx} \quad (7.15)$$

The change in the bed elevation is affected by the subsidence (or uplift) of the alluvial basin. If $\sigma(x)$ is the subsidence rate as a function of the downstream distance x , the sediment continuity equation becomes

$$\sigma(x) + \frac{dh}{dt} = -\frac{1}{1-\lambda} \frac{dq_s}{dx} \quad (7.16)$$

The sediment continuity equation (7.15) can easily be modified for the case of the topography of a hillslope:

$$\frac{\partial q}{\partial x} = -\rho_b \frac{\partial y}{\partial t} \quad (7.17)$$

where q is the discharge of mass per unit width of hillslope, ρ_b is the bulk density of the mobile regolith, x is the horizontal distance from the ridge crest, y is the vertical coordinate, and t is time (Fig. 7.17). The mass discharge per unit width is assumed to be proportional to the local topographic slope by a transport coefficient k , encompassing all of the geomorphic processes acting on the hillslope such as rainsplash, soil creep, bioturbation, overland flow, rilling, and gullyng:

$$q = -k \frac{\partial y}{\partial x} \quad (7.18)$$

The discharge of sediment per unit width is given by equation (7.18) as long as the regolith production rate by weathering (§7.2.2) is sufficiently large. Combining (7.17) and (7.18) gives the familiar diffusion equation

$$\frac{\partial y}{\partial t} = \kappa \frac{\partial^2 y}{\partial x^2} \quad (7.19)$$

where the *diffusivity* $\kappa = k/\rho_b$. This states the familiar result that the erosion or deposition scales on the topographic curvature. The form of a hillslope profile therefore depends on the diffusivity, but the amplitude of the profile is set by the rate of channel incision. Let the incision rate be \dot{e} , and the length of the hillslope from ridge crest to valley bottom L . The steady state profile of the hillslope is obtained by integrating the diffusion equation twice:

$$y = \frac{\dot{e}}{2\kappa} (L^2 - x^2) \quad (7.20)$$

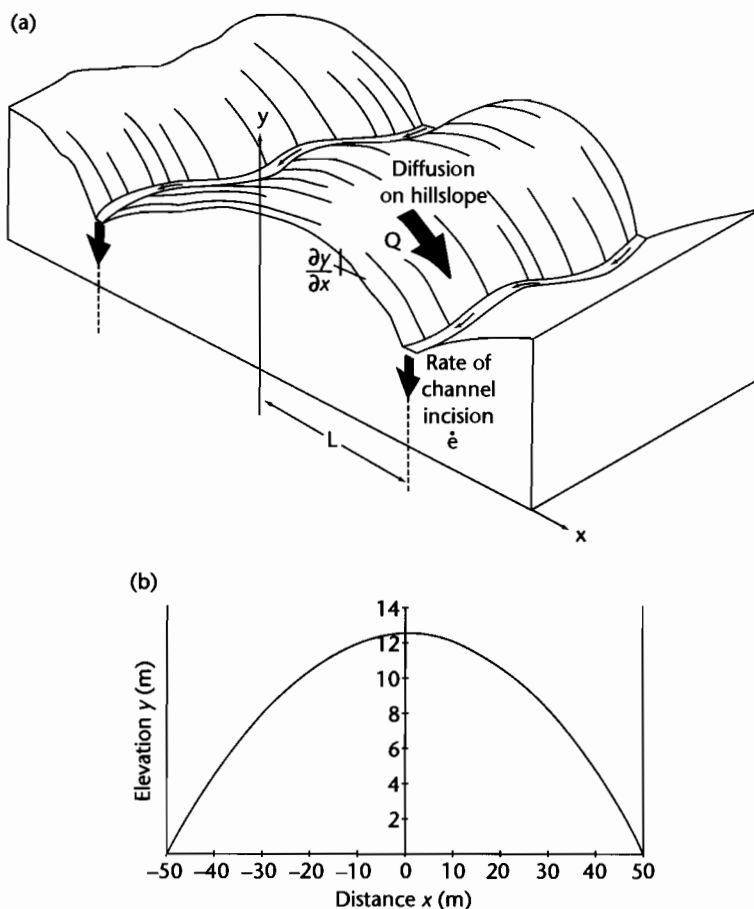


Fig. 7.17 (a) Schematic showing hillslopes and bedrock channels, with notation; (b) Solution (parabolic) for the hillslope profile using the parameter values given in the text.

which shows that the hillslope profile is parabolic. The slope of the hillslope at the ridge crest is zero, and the maximum slope is at the boundary with the river channel (at $x = L$), where it has the value

$$\left| \frac{\partial y}{\partial x} \right|_{\max} = \frac{\dot{e}L}{\kappa} \quad (7.21)$$

The time constant for the hillslope system is given by

$$\tau = \frac{L^2}{\kappa} \quad (7.22)$$

We can use these relationships to predict the hillslope landforms under a range of parameter values (Fig.

7.17b). If two channels located 100 m apart ($L = 50$ m) incise at a rate of 0.5 mm yr^{-1} , typical of tectonic uplift rates, and a diffusion coefficient applicable to the slow processes of rainsplash and soil creep is $50 \times 10^{-3} \text{ m}^2 \text{ yr}^{-1}$, the maximum gradient of the hillslope as given by equation (7.21) is 0.5 ($\tan^{-1} 0.5$ is 27°). The time constant from equation (7.22) is 50 kyr.

Diffusional theory such as presented above can also be used to study the degradation of fault scarps (Hanks et al. 1984), river terraces (Avouac 1993), or independently dated wave-cut lake margin scarps, such as those of Pleistocene Lake Bonneville, Utah. The scarp profile evolves over time by an erosional smoothing of the upper portion and a depositional smoothing of the lower portion. The slope of the midpoint of the scarp decays as the square

root of time, exactly as in the thermal evolution of a piece of newly created oceanic crust (§2.2.4). Diffusivities in the present-day arid landscapes of the American west were estimated as $5\text{--}100\text{ m}^2 \times 10^{-3}\text{ yr}^{-1}$ (Burbank and Anderson 2001). However, a large number of studies suggest that we cannot always assume that the diffusivity κ is constant and independent of x on hillslopes and scarps of various origin. Furthermore, the upper parts of hillslope profiles may be strongly affected by the regolith production rate (§7.2.2), so that they are weathering-limited and therefore not strictly determined by linear diffusion (Rosenbloom and Anderson 1994).

If the channel incision rate is large compared to the diffusive mass wasting of the hillslope, a critical slope will be reached after which landsliding takes place. This is why mountains with high channel incision rates such as the Southern Alps of New Zealand and the Finisterre Range of Papua New Guinea have hillslopes dominated by landsliding. Landslide-dominated hillslopes are straight rather than parabolic (Anderson 1994; Densmore et al. 1997; Densmore and Hovius 2000). The critical slope for the onset of landsliding depends on bedrock strength, vegetation cover, and fluid pressures in the regolith and bedrock. It is likely to vary between $c. 30^\circ$ and 60° . For example, Ellis et al. (1999) found a critical slope for landsliding of just 34° . For the hillslope system above, this critical slope would be achieved at a channel incision rate of 1.2 mm yr^{-1} . For effective diffusivities in the range 10 to $100 \times 10^{-3}\text{ m}^2\text{ yr}^{-1}$, the channel incision rates required to initiate landsliding at critical slopes between 40° and 60° is between $0.2\text{--}3.5\text{ mm yr}^{-1}$. This range covers the tectonic uplift rates of recent mountain belts. The rates of rock uplift along the Alpine Fault in the Southern Alps of New Zealand is over 5 mm yr^{-1} , with rates of 1 mm yr^{-1} along the main drainage divide of the Southern Alps (Koons 1989). The Central Range of Taiwan and the Finisterre Range, Papua New Guinea, have similar tectonic rates of rock uplift.

The flanks of mountain belts are commonly sculpted into transverse valleys and interfluvial ridges with a characteristic spacing (Hovius 1996). The transverse river systems draining linear mountain belts appear to maintain a near constant aspect ratio (Fig. 7.18; Table 7.8)

$$\frac{L_x}{L_z} \approx 2.2 \quad (7.23)$$

where L_x is the length of the main transverse trunk stream and L_z is the width of the catchment or outlet

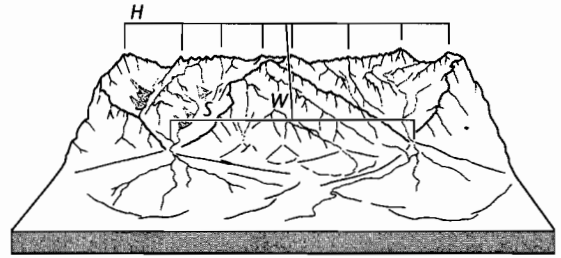


Fig. 7.18 Schematic illustration of two river catchments in a mountainous area with an average elevation of the axial ridge H and half-width W . The catchments have a transverse spacing S at the mountain front, as seen from the locations of the apices of the alluvial fans. Table 7.8 gives data from Hovius (2000).

spacing. In the Southern Alps of New Zealand, the transverse landslide-dominated catchments on the wet western flank have transverse spacings of $5\text{--}10\text{ km}$ and catchment lengths of $20\text{--}25\text{ km}$. Maximum hillslope relief is about 1500 m . What controls this geomorphologic sculpture?

The diffusion equation can be modified to include an advective term to account for the vertical uplift rate of rock:

$$\frac{\partial y}{\partial t} = \kappa \left(\frac{\partial^2 y}{\partial x^2} \right) + V(x) \quad (7.24)$$

where $V(x)$ is the vertical tectonic uplift rate of rock. This diffusion–advection equation can be integrated twice to obtain the height of the hillslopes. We first assume that the landscape is in steady state, so $\partial y / \partial t \rightarrow 0$. Consequently equation (7.24) becomes

$$\kappa \frac{\partial^2 y}{\partial x^2} = -V(x) \quad (7.25)$$

which when integrated is

$$\frac{\partial y}{\partial x} = -\frac{Vx}{\kappa} + c_1 \quad (7.26)$$

Since $\partial y / \partial x = 0$ at $x = 0$, $c_1 = 0$. Integrating (7.26) once again we obtain

$$y = -\frac{Vx^2}{2\kappa} + c_2 \quad (7.27)$$

Table 7.8 Mountain belt geometry and drainage spacing (after Hovius 2000).

Mountain belt	<i>H</i> (m)	<i>W</i> (km)	<i>a</i> (m km ⁻¹)	<i>L</i> (km)	<i>n</i>	<i>S</i> (km)	<i>R</i>
Southern Alps	2653	21.1	123	198	19	10.99	1.92
Finisterre Range	3640	25.5	137	187	15	13.36	1.91
Maoke Range	4038	36.4	108	298	19	16.56	2.20
Barisan Range	1914	28.0	66	439	33	13.72	2.04
Central Range	3292	25.0	124	243	20	12.29	1.95
Kirgizskiy Khrebet	4101	34.7	92	202	14	15.52	2.23
Northern Tien Shan	4950	38.1	84	269	15	19.18	1.99
Apennines	1949	39.2	48	547	33	17.65	2.22
Sierra Nevada	3192	84.0	36	422	12	38.36	2.19
Peruvian Andes	5797	81.9	70	1000	25	40.00	2.05
Central Himalayas	7822	158	49	1610	12	139.2	1.17

Note: *H*, mean height of the culminations of the drainage divide; *W*, average half-width of the mountain belt, measured from the main drainage divide to the mountain front; *a*, mean gradient of the enveloping slope of the range flank; *L*, length of section over which spacing of drainage outlets was measured; *n*, number of streams draining section measured; *R*, aspect ratio of transverse drainages for the section ($R = W/S$). Note that the value of *R* in the central Himalayas is markedly different to the tight clustering of *R* around 2 for the other mountain belts. Anticlines in the Himalayan foothills cause drainage deflection and capture, which amalgamates transverse streams into larger catchments with a wider spacing.

The constant of integration can be found by applying the boundary condition that $y = 0$ at $x = L$. Consequently, $c_2 = VL^2/2\kappa$. Equation (7.27) therefore becomes

$$y = \frac{V}{2\kappa}(L^2 - x^2) \quad (7.28)$$

The maximum height of the hillslope y_{\max} is the height at $x = 0$ minus the height at $x = L$. Consequently,

$$y_{\max} = \frac{VL^2}{2\kappa} \quad (7.29)$$

It is now possible to return to the western flank of the Southern Alps of New Zealand (Koons 1989) (Fig. 7.19) where $L = 3000$ m, $y_{\max} = 1500$ m and V is approximately 5 mm yr^{-1} . The effective erosional hillslope diffusivity must be $15 \text{ m}^2 \text{ yr}^{-1}$. It is considerably higher than the value of $0.01 \text{ m}^2 \text{ yr}^{-1}$ estimated for the semi-arid to arid hillslopes in the western United States (Rosenbloom and Anderson 1994). The effective erosional hillslope diffusivity encompasses a whole range of geomorphologic processes acting on the hillslope, and therefore may lump together the effects of mean annual precipitation (over 12 m yr^{-1}) and rainfall intensity, rock strength, vegetation, and temperature-dependent weathering. The value calculated here reflects the high activity of rapid mass wasting events. The mean gradient of the hillslopes from the diffusion model is y_{\max}/L , which for the Southern Alps examples is 0.5, or 27° . This corresponds closely with measured mean values. Inspection of equation (7.29)

shows that the transverse spacing of hillslopes must always be small in order to balance high rates of tectonic uplift of rock in a steady state landscape. On the drier eastern flank of the Southern Alps ($<1 \text{ m yr}^{-1}$ mean annual precipitation) the tectonic uplift rates reduce from 1 mm yr^{-1} at the main divide to zero at the east coast of South Island. On this flank, braided river valleys are broadly spaced and less deeply entrenched into bedrock.

From equation (7.29), the aspect ratio of y_{\max}/L can also be written as $VL/2\kappa$. This is a dimensionless ratio of a flow rate of rock across a section of the transverse drainage versus an effective erosional diffusivity. It has the form of a *Peclet number*. If the *erosional Peclet number* is greater than about 0.6, it is unlikely that erosional processes can keep pace with tectonic uplift rates to produce a steady state landscape. The erosional Peclet number for the wet western flank of the Southern Alps using the parameter values above is 0.5.

7.5.2 River incision

The products of hillslope erosion are transported away by channelized flows (rivers). Channelized flow takes place wherever a stream power threshold is locally exceeded (Montgomery and Dietrich 1988). There is a fundamental distinction, however, between rivers incised into bedrock (this section) and alluvial rivers with beds and banks of sediment (§7.5.3). Bedrock rivers are those that lack a coherent bed of active alluvium (Howard

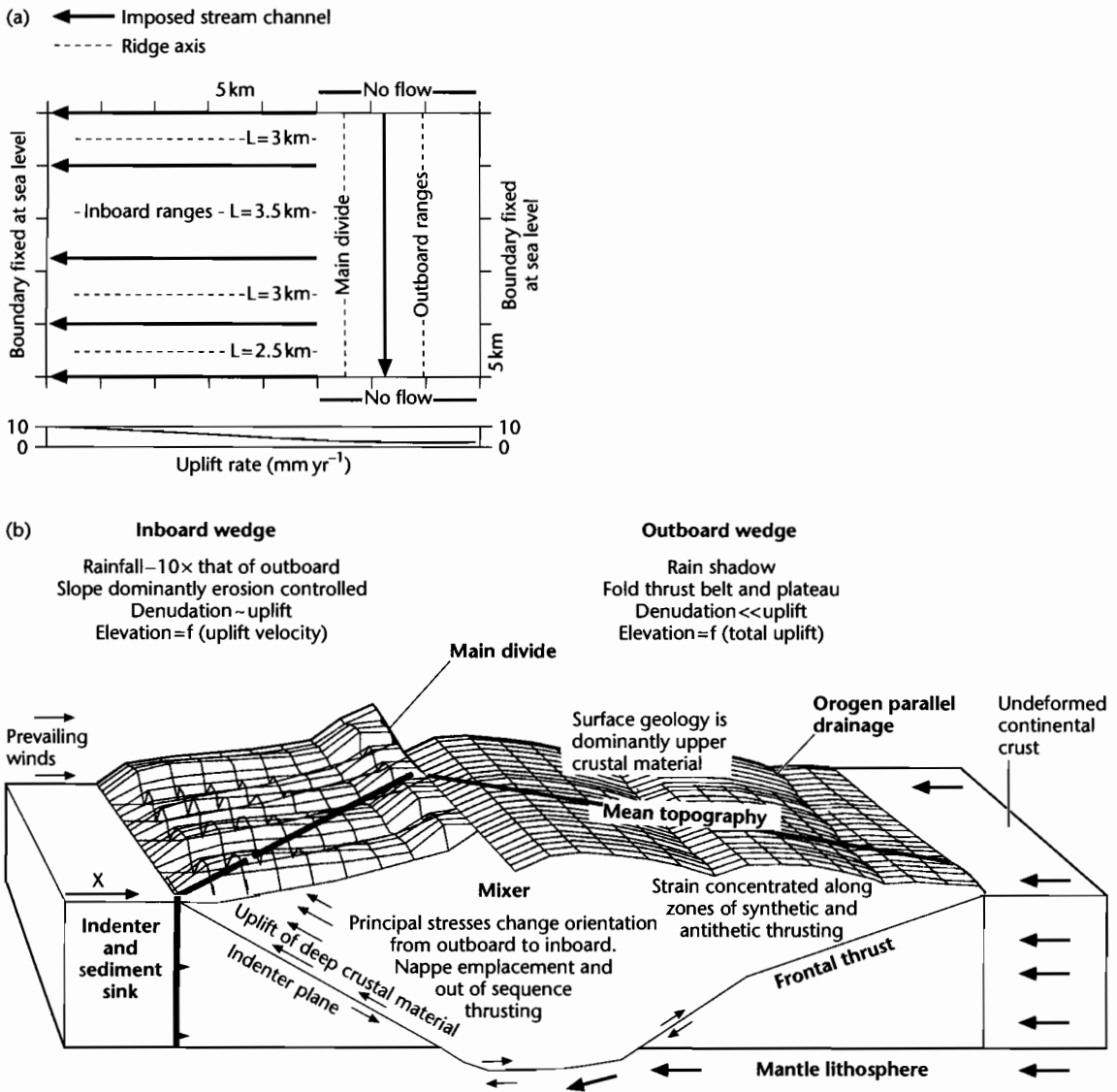


Fig. 7.19 The doubly vergent orogenic wedge of the Southern Alps has deeply etched, narrowly spaced, transverse drainages on the wet, western flank where tectonic uplift rates are high. On the drier eastern flank, rivers are much less deeply entrenched and are broadly spaced. (a) Boundary and initial conditions for the numerical model in Koons (1989); (b) Plate velocities outside the wedge, tectonic transport directions within the wedge, and surface topography for a doubly vergent wedge with precipitation from the left. The marked asymmetry in denudation promotes a strong asymmetry in rock uplift within the wedge. Modified from Koons (1989).

1987). Consequently, bedrock rivers have a transport capacity that is larger than that required to transport all of the available sediment. They incise by abrasion by the sediment load, plucking of blocks from the bed and cavitation (Hancock et al. 1998). Bedrock rivers are the dominant channel type in mountainous topography.

There are a number of interrelated ways of approximating the rate of bedrock incision. A common approach makes use of the idea that bedrock incision is controlled by an area-slope or discharge-slope product. This is often termed the *stream power rule* (Boxed text 7.2). A related view (Howard 1994) is that the rate of bedrock

BOXED TEXT 7.2: Use of the Stream Power Rule

Consider a volume V of water, density ρ_w , in a river that moves downstream changing its elevation by dy over a lateral distance dx in a time period dt . There is a change in potential energy caused by this downstream motion. If we assume that the mass of water ($V\rho_w$) does not change, this change in potential energy is $V\rho_w g dy$. The rate of change of energy loss, or power, is simply $V\rho_w g dy/dt$. Now the volume of water moving through the river per interval of time dt is Q_w/dt , where Q_w is the water discharge. Consequently, the stream power per length of stream channel dx is given by

$$P/dx = kQ_w \frac{dy}{dx} \quad (7.30)$$

where the coefficient $k = \rho_w g$. The stream power (per length of stream channel) is therefore proportional to a discharge-slope product. The rate of bedrock incision is conventionally assumed to have the form of a power law version of equation (7.30)

$$\frac{\partial y}{\partial t} = -c_b Q_w^m S^n \quad (7.31)$$

where Q_w is the total discharge of water, S is the slope, m and n are empirical coefficients and c_b is a bedrock incision coefficient. The parameters contributing to the value of the bedrock erosion coefficient c_b remains debatable. In the simplest case, let us assume that it is a constant determined by lithology, ranging from 7×10^{-3} for mudstones to 6×10^{-6} for granite and basalt (Stock and Montgomery 1999).

The discharge of water in the channel depends on the drainage area upstream of the stream channel A , the average precipitation over the area P , and a run-off coefficient C , that accounts for transmission losses through the hillslope-channel system (§7.3) ($Q_w = CAP$). If the long-term effective discharge varies linearly with drainage area, then $m = n = 1$ and the incision rate is then linearly proportional to stream power (Seidl and Dietrich 1992).

The drainage area upstream of a particular point in the channel increases with distance down the channel,

and on the basis of empirical results (Montgomery and Dietrich 1992) is well described by

$$A = \frac{x^2}{3} \quad (7.32)$$

Consequently, the rate of channel incision can be expressed as

$$\frac{\partial y}{\partial t} = -c_1 x^2 S \quad (7.33)$$

where c_1 is a coefficient equal to $c_b PC/3$. It can be seen therefore that in a bedrock valley where the width of the stream does not change significantly in the downstream direction, the rate of bedrock incision varies by the square of the distance from the drainage divide x and the single power of the slope S . These two effects are traded off against each other. The result is that the rate of valley incision increases to a maximum at a certain distance from the drainage divide.

However, theory and empirical data suggest that m/n is ~ 0.5 , and analysis of the topography of the Zagros fold and thrust belt (Tucker 1996) indicates that m and n are $1/3$ and $2/3$ respectively. In such a case, the rate of bedrock channel incision becomes

$$\frac{\partial y}{\partial t} = -c_2 x^{2/3} S^{2/3} \quad (7.34)$$

where c_2 is equal to $c_b(PC/3)^{1/3}$.

It is also possible that the bedrock erosion coefficient is a more complex function of hydrological variables, including the flow resistance of the bed. The channel incision rate can also be expressed in terms of an "erosional velocity" c_v (units of m s^{-1}), so that

$$\frac{\partial y}{\partial t} = -c_v \left(\frac{Q_w}{Q^*} \right)^m S^n \quad (7.35)$$

where Q^* is a characteristic channel discharge (equal to the total area of the catchment times the average precipitation rate, Tucker and Slingerland 1996).

incision is proportional to the shear stress on the bed. Alternatively, the rate of incision could be related to the excess stream power available to erode bedrock in the channel bed above that required for sediment transport (Seidl and Dietrich 1992). For simplicity we illustrate the modeling of bedrock incision using the area-slope or discharge-slope product in Boxed text 7.2.

Hillslopes and bedrock channels are dynamically linked, but they have different response times. The hillslope response time is L^2/κ (eqn 7.22). The response time of the channel system must be influenced by the length of the channel and the average velocity of the knick-points generated when the channel adjusts to its new base level. Such knickpoints migrate headwards, but slow down in their upstream velocity as the stream power decreases due to a reduction in the contributing drainage area. Anderson (1994) calculated channel system response times assuming the stream power rule as typically 10^3 – 10^4 yr. This is significantly longer than the response time for landslides, but is comparable to the hillslope response time. This suggests that hillslopes characterized by the high effective diffusivities produced by landslides are always in equilibrium with the incising channels. Less steep hillslopes dominated by slow diffusion, however, may not be in equilibrium with channel incision and may display transient rather than steady state morphologies.

We saw in §7.4.1 that deep incision by rivers causes a removal of mass from the area undergoing erosion, which drives an isostatic compensation (Molnar and England 1990). Consequently, the high mountain peaks fringing deeply incised valleys may experience a surface uplift. We can now restate this possibility in terms of a bedrock river incision rule. Assuming the isostatic uplift to be due to a local (Airy) compensation rather than to a regional flexure (Chapter 4), the rate of uplift of the mountain peaks is

$$\frac{\partial y_p}{\partial t} = \frac{1}{2} \left(\frac{\rho_c}{\rho_m} \right) c_1 x^2 S \quad (7.36)$$

where ρ_c and ρ_m are the crustal and mantle densities respectively. Using $c_1 = 0.5 \text{ m}^{-1} \text{ Myr}^{-1}$, profiles along the Arun and Karnali Rivers in the Nepalese Himalaya show the elevation of mountain peaks some distance downstream from the drainage divides in the Tibetan Plateau (Montgomery 1994) (Figs. 7.20, 7.21). The greatest relief is on the edge of the Himalayan Plateau, where the Karnali River has incised 4500 m below the surrounding peaks. As much as 20–30% of the present elevation of the Himalayan peaks can be explained by isostatic compensation.

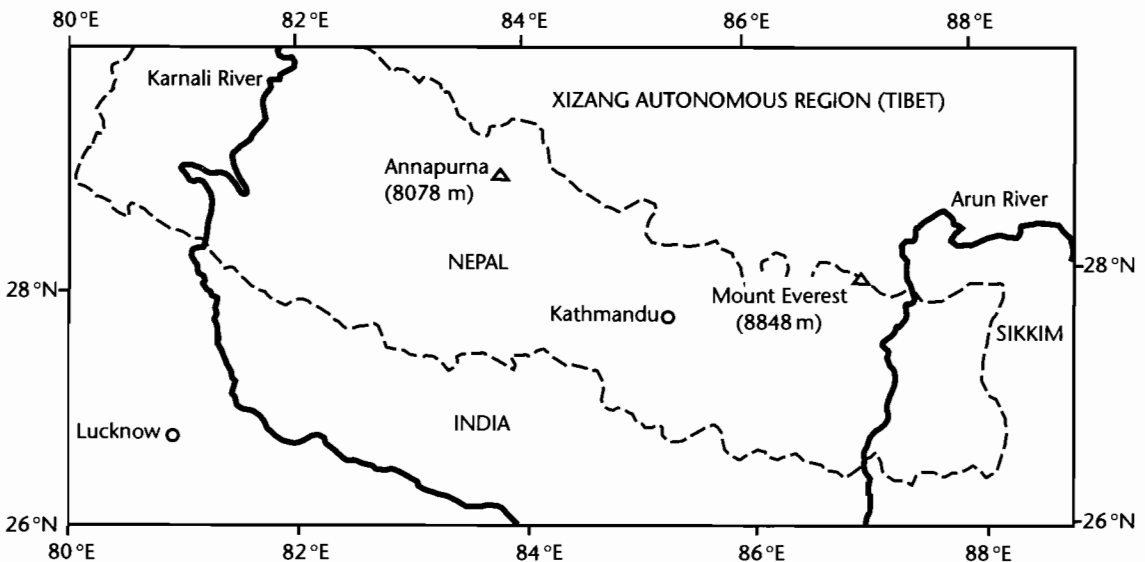


Fig. 7.20 The Himalayas and Tibetan Plateau, with location of Arun and Karnali Rivers.

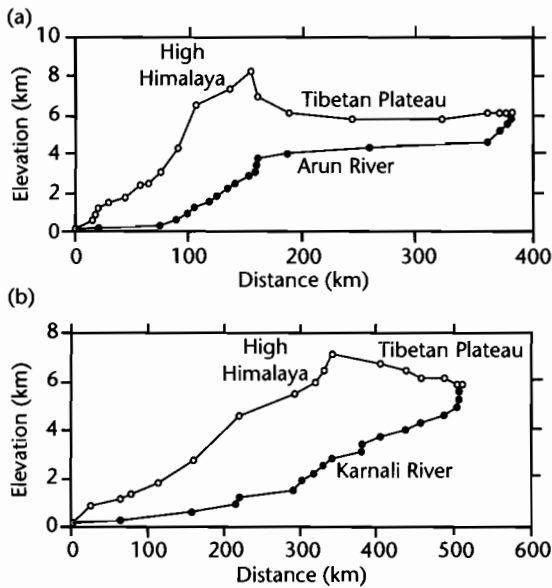


Fig. 7.21 Long profiles of the mountain peaks and valley bottoms along the Arun (a) and Karnali (b) rivers, showing the high elevation of the summits *c.* $x = 200$ km from the headwater regions, suggesting that bedrock river incision rates produce an isostatic uplift of the peaks. After Montgomery (1994). Reproduced courtesy of American Geophysical Union.

7.5.3 Long range fluvial transport

A fundamental characteristic of alluvial channels is that they have sufficient sediment to equal or exceed the transport capacity. The transport of sediment in river systems has been the subject of modeling by a generation of civil engineers, geomorphologists, and latterly, geologists. Our purpose here is not to attempt a full description of long range sediment transport by rivers. For more comprehensive treatments the reader is referred to Parker (1978a, b), Paola et al. (1992) and Dade and Friend (1998).

Various forms of diffusion equation of the type given in equation (7.24) have been applied to long range fluvial transport. Here we concentrate on an assessment of long range fluvial transport of a mixture of gravel and sand. The quantitative development of this group of models can be found in Paola et al. (1992) and Marr et al. (2000). It is well known in modern mixed gravel-sand fluvial systems that there is a relatively steep gravelly proximal zone with an abrupt change to a lower gradient sandy zone (Sambrook-Smith and Ferguson 1995). To be able

to predict the movement of the “gravel front,” or “gravel-sand transition” would be of considerable benefit in basin analysis.

Most models of sediment transport in rivers make the same set of assumptions.

1 First, it is assumed that the long term flow of water in a river approximates that of a steady uniform flow down an inclined plane. For a flow of depth h and density ρ on a slope $\delta y/\delta x$, the downslope component of the fluid weight on a unit area of the river bed is $\rho gh \delta y/\delta x$. This downslope acting force must be opposed by an equal and opposite drag force exerted on the fluid by the unit area of bed – this is the shear stress τ_0 (Fig. 7.22a). Consequently, the force balance gives

$$\tau_0 = -\rho gh \frac{\partial y}{\partial x} \quad (7.37)$$

Rivers are anything but steady and uniform. However, equation (7.37) can be used as an approximation for long-term river behavior. It works best for shallow high-gradient streams and worst for deep, low-gradient streams. If the flow depth is large compared to the channel width, h should be replaced by the *hydraulic radius* R in equation (7.37) (Fig. 7.22b).

2 Second, we make use of an equation that expresses the resistance to flow in the channel. A fluid moving over its bed and banks experiences frictional losses of energy known as *flow resistance*. Where the bed of the river is rough, as is always the case in natural rivers, the energy losses should in some way be related to the length scale of the roughness of the bed. This roughness can be expressed in a number of ways. A common method is to use the *Darcy-Weisbach friction factor* f

$$f = \frac{8\tau_0}{\rho_f u^2} \quad (7.38)$$

where u is the flow velocity. The friction factor (or similar forms such as the Chézy coefficient C and Manning’s n) varies strongly according to the grain size of the sediment on the river bed and is especially affected by the presence of bedforms such as ripples and dunes and of macroforms such as bars, chutes, and pools.

3 Third, we conserve the discharge of water through the system. Consider a slice of width B of an alluvial basin of length L , which has active channels on its surface with

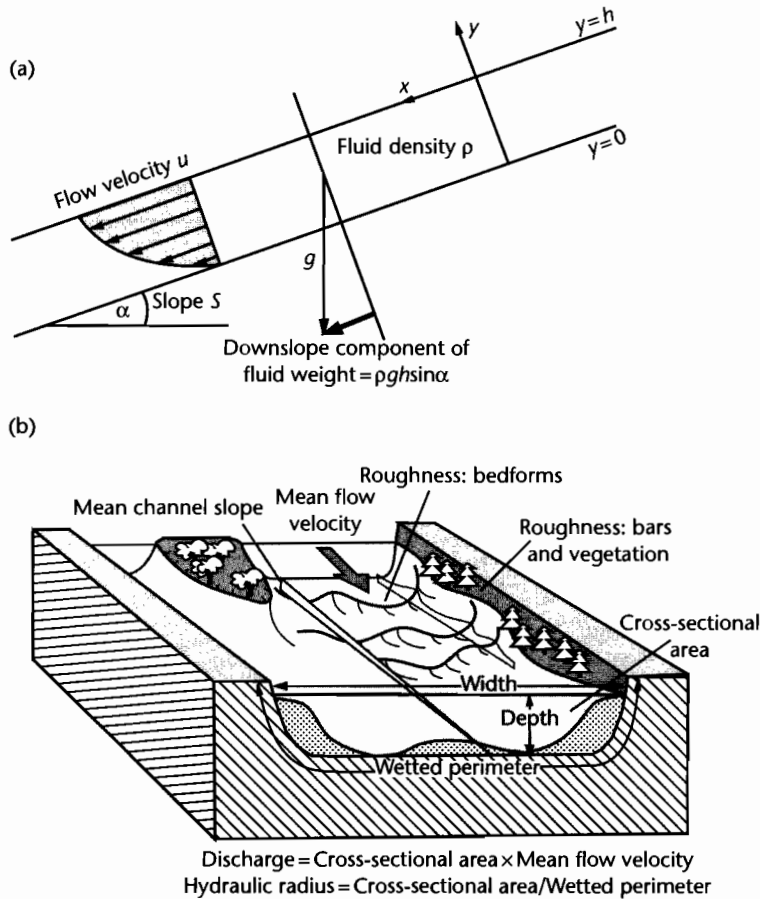


Fig. 7.22 (a) Notation for steady uniform flow down an inclined plane of slope $\sin \alpha$; (b) The wetted perimeter and hydraulic radius of a river. The presence of bar forms, pools, dunes and ripples, vegetation, and pebbles all contribute to the friction factor of the river.

cumulative width b , of flow depth h and containing flows of velocity u (Fig. 7.23). Let β be the fraction of the section width B occupied by channels, so $\beta = b/B$. The discharge of water Q_w in the channels occupying the width of floodplain B is bhu , or averaged across the floodplain is βhu . Consequently,

$$\beta = \frac{Q_w}{hu} \quad (7.39)$$

4 Finally, we make use of the sediment continuity equation (7.16), modified by the use of a dimensionless shear stress τ_* , as given by Shields

$$\tau_* = \frac{\tau_0}{(\rho_s - \rho_f)gD} \quad (7.40)$$

where D is the median grain size and ρ_s and ρ_f are the sediment and fluid densities respectively. There appear to be strong limits on the value of the dimensionless shear stress, so that it can be treated as a constant, at about 1.4 times the critical shear stress at the threshold of particle motion in coarse-grained braided rivers, and between 1 and 2 in alluvial sand-bed rivers (Paola and Seal 1995; Dade and Friend 1998; Parker et al. 1998). It is probably a constant because if it is too high, the stream erodes its banks and widens its bed, thereby reducing the shear

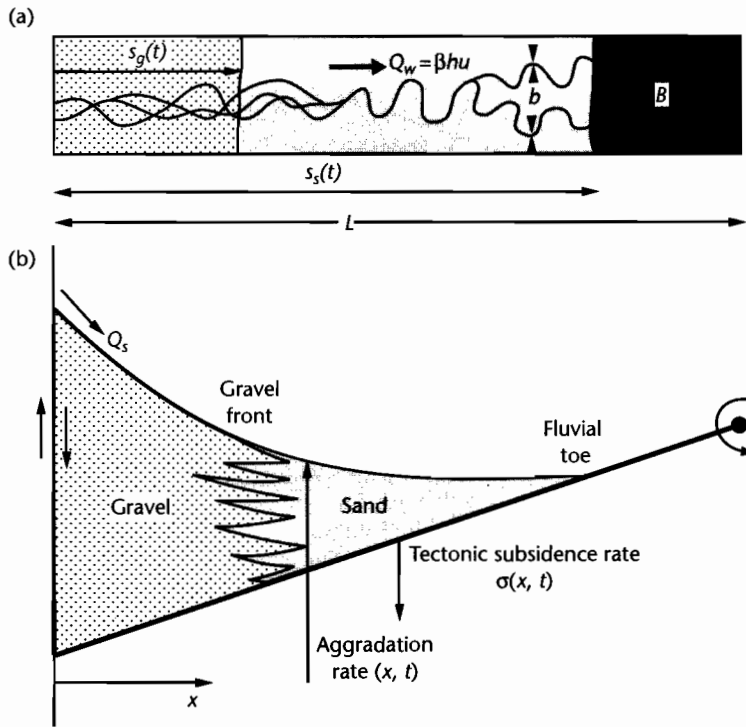


Fig. 7.23 Map view and cross-section of a slice of alluvial basin of length L , width B , containing channels with cumulative width b undergoing tectonic subsidence $\sigma(x)$ approximated by a linear tilt from a distant hinge. Note the break in slope at the gravel front and the position of the fluvial toe. After Marr et al. (2000). Reproduced courtesy of Blackwell Publishing Ltd.

stress per unit area of stream bed (Parker 1978a, b). There is a sharp jump in τ at the gravel–sand transition or “gravel front” in many rivers. The modified sediment continuity equation therefore has the form

$$\frac{\partial y}{\partial t} = \frac{\partial}{\partial x} \left(\kappa \frac{\partial y}{\partial x} \right) - \sigma(x) \quad (7.41)$$

where the effective diffusivity or transport coefficient κ of the alluvial system is dependent principally on the discharge of water, a friction (flow resistance) factor, a dimensionless sediment transport rate, and the dimensionless shear stress. The transport coefficient is constant within the gravel and sand regimes, but changes by a factor of about 10 at the boundary. Typical values for κ used by Marr et al. (2000) are $0.01 \text{ km}^2 \text{ yr}^{-1}$ in the gravel regime and $0.1 \text{ km}^2 \text{ yr}^{-1}$ in the sand regime.

The simplest approximation of the time required for equilibrium to be achieved with a set of forcing condi-

tions, or *basin response time* T_{eq} , is L^2 / κ , where L is the basin length, as in the diffusional problems previously encountered. In a two-diffusion model, the gravel and sand regimes may have their own response times. For a basin length of 100 km and κ for gravel of $0.01 \text{ km}^2 \text{ yr}^{-1}$, the response time is 10^6 yr , whereas with κ for sand, we have a response time of 10^5 yr . An important parameter should be the period of the forcing T compared to the basin response time T_{eq} . Marr et al. (2000) considered cross-sections of basin stratigraphy under different conditions of forcing, using the total sediment flux Q_s , the water discharge Q_w , the gravel fraction f_g , and the rate of tectonic subsidence σ . When the forcing variable has a rapid sinusoidal change (for example, in sediment supply), $T \ll T_{eq}$, the time for equilibrium to be re-established is almost constant for a fixed gravel fraction, suggesting that the basin response time is controlled by the fluvial system rather than the frequency of the forcing. The value of this *intrinsic* response time is determined by the gravel fraction (fast – $< 10^5 \text{ yr}$ – with low gravel fractions and

slow – 10^5 – 10^6 yr – for high gravel fractions). In the simulations found in Figures 7.24 and 7.25, slow forcing is $T = 10^7$ yr, whereas fast forcing is $T = 10^5$ yr. The important aspects for basin analysis are as follows.

With *slow forcing* (Fig. 7.24):

- 1 The movements of the sand toe and gravel front are in phase with variations in sediment flux, with proximal and distal accumulation of sediment both occurring at the time of high sediment flux. Retreat of the fluvial toe at times of low sediment flux produces distal unconformities.
- 2 During periods of increased subsidence, sediment is trapped in proximal regions and distal areas are starved, causing a retreat of both the gravel front and the fluvial toe and the creation of distal unconformities. During periods of reduced subsidence rate, the gravel front and fluvial toe prograde since accommodation is reduced. Both proximal and distal accumulation are therefore out of phase with subsidence rate.
- 3 The position of the gravel front moves outwards when the gravel percentage (for a constant sediment flux) increases, producing a coarsening up in a vertical section.

For *rapid forcing* (Fig. 7.25):

- 1 Rapid changes in sediment flux produce gravel and sand regions with markedly different slopes, and the position of the gravel front is out of phase with the forcing. Reduced sediment supply causes a reduction in proximal slopes, the cutting of proximal unconformities and the progradation of the gravel front. In contrast, reduced sediment supply causes the fluvial toe to retreat. During periods of increased sediment supply, proximal slopes increase, which causes the gravel front to retreat, while the fluvial toe progrades slightly.
- 2 Rapid variations in subsidence rate have little effect on the gravel front.
- 3 The position of the gravel front and proximal accumulation are in phase with the percentage gravel fraction.

It is clear therefore that the stratigraphy of an alluvial system exhibits a complex response to the various forcing mechanisms. The response of the system depends on the time scale of the forcing compared to the basin response time T/T_{eq} . Proximal and distal unconformities, variations in proximal and distal accumulation and movements of the gravel front and fluvial toe may be in phase or out of phase with external forcing.

The response times of alluvial systems have also been approximated from measurements of the sediment discharge leaving the catchment. River basins may have extensive floodplain areas in their downstream portions,

which act as buffers to changes in any forcing variables, such as base level change at a river mouth, or changes in sediment flux near their headwaters, and therefore may have long response times. If the system is assumed to be diffusive in character, and the discharge of water varies systematically with floodplain width W , the mass effective diffusivity κ of the channel–floodplain system is

$$\kappa = \frac{Q}{W \left\langle \frac{\partial y}{\partial x} \right\rangle} \quad (7.42)$$

where Q is the sediment discharge and $\langle \rangle$ denotes the spatial average of the slope. If L is the downstream length of the river–floodplain system and H the maximum relief between its upstream and downstream ends, the response time becomes

$$\tau = \frac{L^2}{\kappa} = \frac{L^2 W \langle \partial y / \partial x \rangle}{Q} = \frac{LWH}{Q} \quad (7.43)$$

The large river systems of Asia have typical values of $L \sim 10^6$ m, $W \sim 10^5$ m, $H \sim 1\text{--}2 \times 10^2$ m (slopes of 10^{-3} to 10^{-4}), and sediment discharges Q of $10^{7\text{--}8}$ m³ yr⁻¹ (Métivier and Gaudemer 1999). The characteristic response time is therefore in the region of 10^5 to 10^6 years. Castelltort and Van Den Driessche (2003) carried out a similar analysis on 93 of the world's major rivers, and found that response times varied between 10^4 yr to more than 10^6 yr. (Fig. 7.26). The response time depends on the scale of the channel–floodplain system. As we saw in the forward modeling of alluvial stratigraphy above, large alluvial systems therefore strongly buffer any variations in sediment supply with frequencies of less than $10^{5\text{--}6}$ years. This has strong implications for the detection of high frequency driving mechanisms in the stratigraphy of sedimentary basins.

7.5.4 Some aspects of numerical landscape evolution models

The numerical modeling of landscapes has developed over the last couple of decades. The significance of numerical landscape evolution for basin analysis is that such models allow the sediment supply to basins to be simulated in terms of tectonic, climatic, and geomorphic sets of rules. The incorporation into a physically realistic numerical model of feedbacks between the various processes that shape a landscape also allows system behavior, such as the response time to a change in a

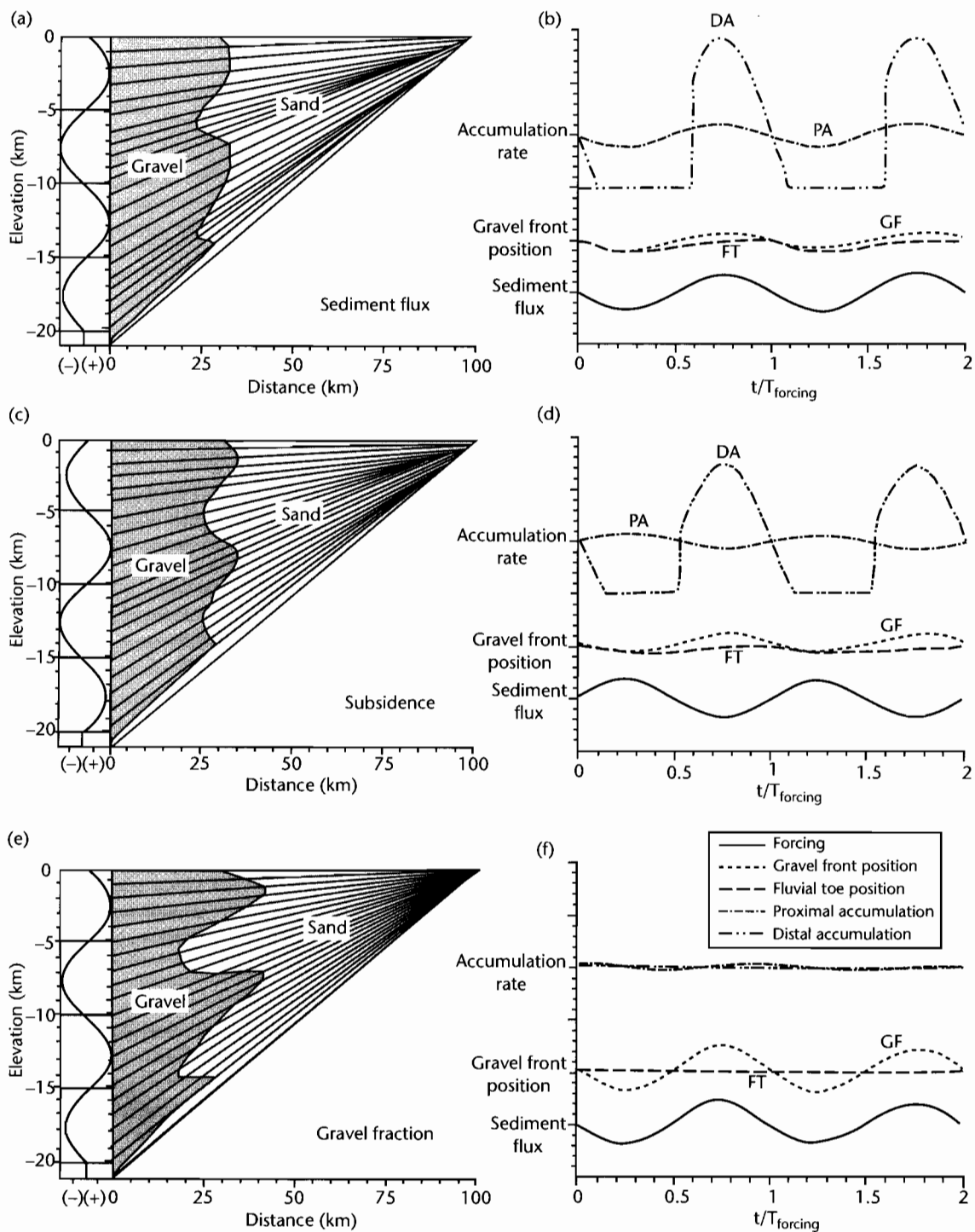


Fig. 7.24 Cross-sections of alluvial stratigraphy under slow sinusoidal forcing ($T > T_{eq}$) of sediment flux (a), tectonic subsidence (c) and gravel fraction (e). Diagrams on right (b, d, f) show time variation of the position of the gravel front and fluvial toe, proximal and distal accumulation and the forcing variable. Further details can be found in Marr et al. (2000). GF, gravel front; FT, fluvial toe; DA, distal accumulation; PA, proximal accumulation. Reproduced courtesy of Blackwell Publishing Ltd.

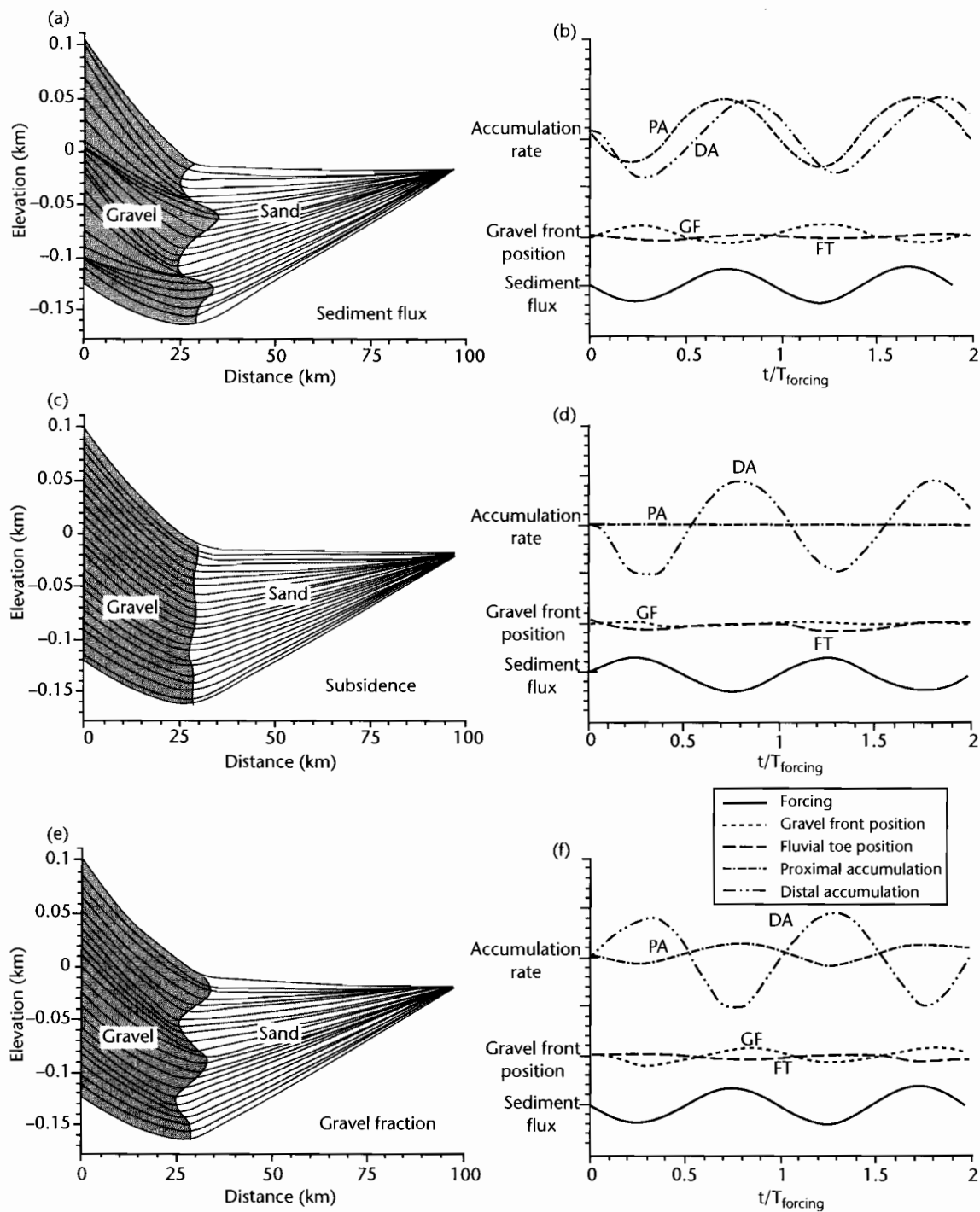


Fig. 7.25 Cross-sections of alluvial stratigraphy under fast sinusoidal forcing ($T < T_{\eta}$) of sediment flux (a), tectonic subsidence (c), and gravel fraction (e). Diagrams on right (b, d, f) show time variation of the position of the gravel front and fluvial toe, proximal and distal accumulation and the forcing variable. Further details can be found in Marr et al. (2000). Reproduced courtesy of Blackwell Publishing Ltd.

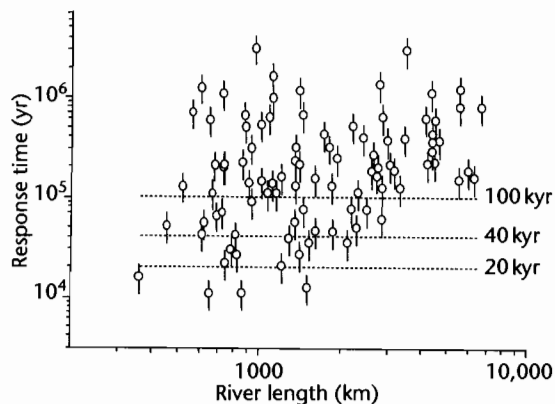


Fig. 7.26 Response times of some modern drainage basins, from a dataset compiled by Castelltort and Van Den Driessche (2003) using the relations given in equations (7.42) and (7.43). Hydrologic and geomorphologic data from Hovius (1998). Response time is plotted against river length. Vertical bars show uncertainties based on the unknown bedload sediment transport rates of the rivers shown. Note that the majority of response times are $>10^5$ yr, and some are $>10^6$ yr. Reproduced courtesy of Elsevier.

driving mechanism or forcing variable, to be studied. Numerical landscape models range in their spatial and temporal scales, from whole contractional orogens and passive margin mega-escarpments (length scales of ~ 100 km and time scales of $\sim 10^7$ yr) to individual extensional fault blocks or thrust-related anticlines (length scales of ~ 10 km, time scales of $\sim 10^6$ yr), and even to the fault scarps generated by single seismic events (length scale of ~ 100 m, time scales of 10^3 – 10^5 yr). The resolution (of the elevation of topography) required by the landscape evolution model varies accordingly, from cm in the case of a degrading fault scarp, to ~ 100 m for an orogen. The spatial and temporal scale and topographic resolution commonly affect the way in which tectonic and geomorphic processes are dealt with in the numerical model. Burbank and Anderson (2001) provide a useful summary. Many of the algorithms used in numerical landscape models are identical to or similar to those given in §7.5.1–§7.5.3. We concentrate here on the intermediate scale of extensional fault blocks and anticlinal folds in fold–thrust belts.

7.5.4.1 Tilted extensional fault blocks and thrust-related anticlines

Early attempts to model the evolution of simple fault-bounded ranges used a single planar fault with uniform

slip, diffusional modification of the tectonically generated topography using a single, constant value of κ , and flexural compensation (King et al. 1988; Stein et al. 1988). Later models incorporated channels and hillslopes that strongly interacted (§7.5.1 and §7.5.2), with transport rules for the disposal of sediment derived from hillslope erosion, and hillslopes were allowed to fail by landsliding (Densmore et al. 1998; Ellis et al. 1999). Such models not only simulated very realistic landscapes in the Basin and Range Province of SW USA, but also allowed system behavior to be better evaluated. These tectonic–geomorphic systems involve steep transverse drainage systems over uplifting footwall blocks, with fans in the neighboring hangingwall basins (Whipple and Trayler 1996; Allen and Hovius 1998). The area of the catchment acting as a source terrain for sediment A_1 , relative to that of the hangingwall fan A_2 , is an indicator of how this relatively simple tectonic–geomorphic system functions (Fig. 7.27).

We introduce a dimensionless proportionality coefficient V , following Allen and Hovius (1998), which incorporates all the various processes resulting in the transport of sediment eroded from the catchment, routed to the fan head and then distributed across the fan with a spatially averaged deposition rate j :

$$\phi = \frac{1}{j} V \frac{(1-\lambda_r)}{(1-\lambda_s)} e_s e_f \quad (7.44)$$

and

$$A_1 = \phi A_2 \quad (7.45)$$

where V is the sediment efflux of the catchment, λ_r and λ_s are the porosities of rocks in the catchment and sediments on the fan respectively, e_s is an efficiency factor accounting for temporary storage of sediment within the catchment, and e_f is an efficiency factor allowing for escape of some sediment from the fan into down-fan sabkhas, lakes, or axial river systems. In the simplified case of complete evacuation of the catchment with no storage ($e_s = 1$) and a closed system for sediment delivery to the fan ($e_f = 1$), and assuming that rock and sediment porosities are comparable ($\lambda_r \approx \lambda_s$), equations (7.44) and (7.45) simply illustrate that ϕ depends strongly on the rate at which the fan aggrades, which is controlled fundamentally by the rate of tectonically created accommodation. Consequently, tectonics play a major role in the creation of uplifting footwalls as source regions for sediment, in determining the spatial pattern and rate of hangingwall subsidence, and thereby in controlling fan

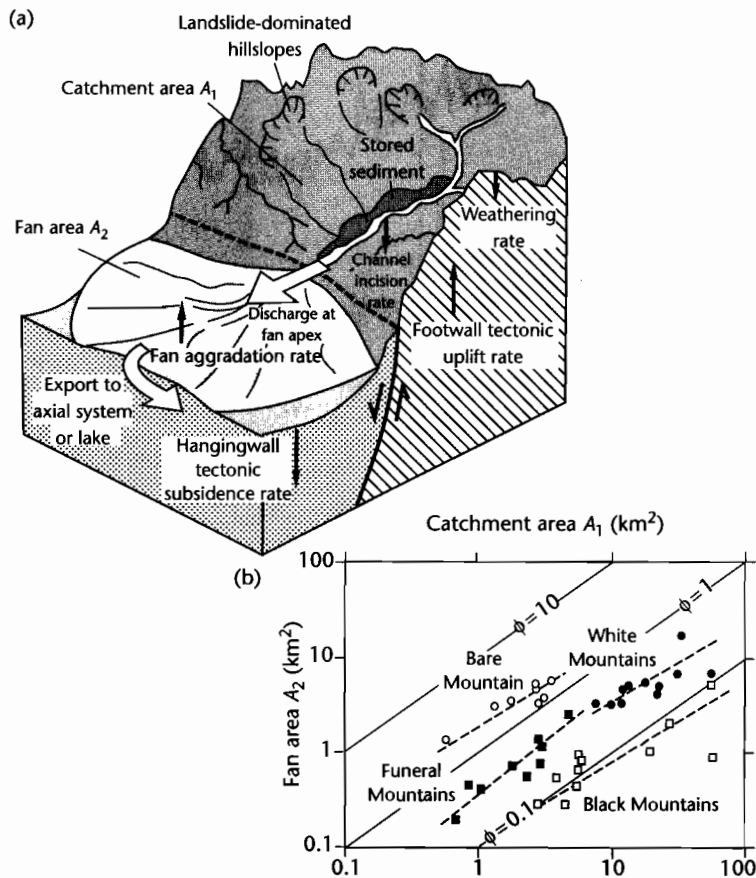


Fig. 7.27 (a) Schematic illustration of a catchment-fan system associated with a tilted extensional fault block (after Allen and Hovius 1998, Allen and Densmore 2000); (b) shows plot of catchment area A_1 versus fan area A_2 for catchment-fan systems in the arid southwestern US, showing that individual regions with particular slip rates are discriminated in terms of their value of ϕ .

thickness and fan progradation distance. Not surprisingly, plots of fan area versus catchment area from examples in the arid SW USA (Allen and Hovius 1998) show that areas with high fault displacement rates and areas with low fault displacement rates are discriminated by their value of ϕ (Fig. 7.27b). This implies that coarse-grained fan bodies are stacked against active range-bounding faults, whereas fans coalesce and prograde basinwards where fault displacement rates are smaller.

Using the landscape evolution model developed by Densmore et al. (1998), Allen and Densmore (2000) showed that abrupt changes in the rate of slip on range-bounding extensional faults could be recognized by changes in mean catchment erosion rate and mean fan deposition rate (Fig. 7.28), but that there was a delay in

the achievement of a new steady state under the new fault slip rate conditions. This response time was ≈ 50 kyr for the catchment-fan systems in the Death Valley region of eastern California, regardless of climatic conditions. In other words, changes in the tectonic boundary conditions at a frequency of less than 50 kyr will be difficult to recognize in the stratigraphic record.

The deforming crustal template in regions of extension strongly interacts with erosion and drainage development. As footwalls emerge, river systems are etched into their flanks either side of a catchment divide. Individual *en echelon* fault segments interact at their tips in a variety of geometrical arrangements, most important of which is the *relay zone* (Larsen 1988). These relay zones are thought to have an important role in focusing

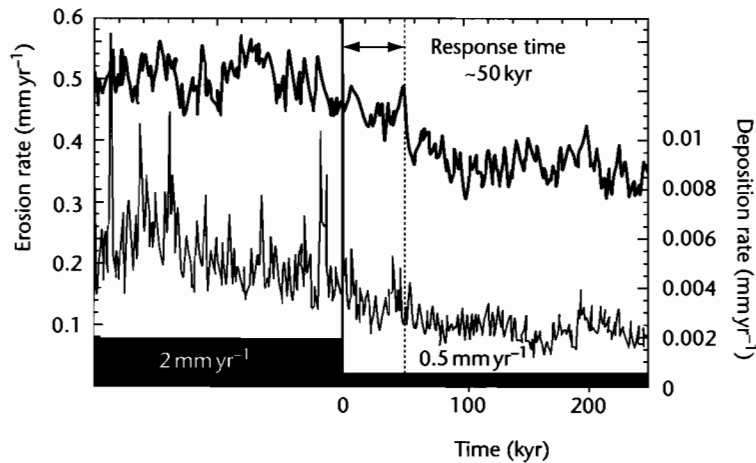


Fig. 7.28 Mean catchment-averaged erosion rate (heavy line) and mean fan deposition rate (thin line) before and after a step change in fault slip rate from 2 mm yr^{-1} to 0.5 mm yr^{-1} . Note the progressive decrease in erosion and deposition rates to new equilibrium values. The response times (the time required for each rate to fall to $1/e$ of its initial value) are 56 kyr for erosion rate and 48 kyr for deposition rate. After Allen and Densmore (2000). Reproduced courtesy of Blackwell Publishing Ltd.

sediment delivery to hangingwall basins from larger-than-normal catchments and are therefore thought to be associated with fan and fan-delta development (Leeder and Gawthorpe 1987; Gupta et al. 1999) (Fig. 7.29). Such sedimentary bodies adjacent to relay zones are potentially important as hydrocarbon reservoirs in rift provinces (§10.4). However, numerical landscape evolution models of fault systems under different histories of growth and linkage failed to produce large catchments and fans at relay zones (Densmore et al. 2003). This suggests that large catchment-fan systems at relay zones may be related to antecedent drainage rather than to local fault growth. Whereas the Basin and Range is typified by hydrologically closed footwall catchment systems, in which we do not expect to find large catchment-fan systems at relay zones, other extensional provinces may possess regional, antecedent drainages that deposit large fans at relay zone entry points into hangingwall depocenters, such as the southern Afar Rift, Gulf of Suez, and central Greece.

At a similar wavelength to the extensional fault blocks of the Basin and Range are the thrust-related folds of contractional tectonic provinces such as the Zagros of Iran and western Pakistan (Mann and Vita-Finzi 1988). Folds are $c. 10 \text{ km}$ in wavelength and $2\text{--}3 \text{ km}$ in amplitude. There are a number of issues that are especially relevant to this tectonic situation: as hangingwall rocks

are transported up the thrust ramp, how is the topographic profile and river drainage development related to the tectonic paths of hangingwall rocks? What is the effect of progressively unroofing rocks with markedly different erodibilities (or values of c_b or c_r)? And what effects do the contractional tectonics have on antecedent rivers?

In areas with high rates of tectonic uplift of rocks, the topographic relief is essentially controlled by the ratio U/c_r , where U is the tectonic uplift rate of rock and c_r is the efficiency of bedrock incision expressed as a velocity (eqn 7.35). Streams are known to change their gradients markedly over substrates of different erodibility (Hack 1973). Tucker and Slingerland (1996) estimated bedrock erodibilities c_r to vary from 0.02 m yr^{-1} to 0.2 m yr^{-1} in the arid landscapes of the Zagros. Using a numerical landscape evolution model, they successfully simulated the progressive unroofing of stratigraphy with strongly varying erodibility related to the growth of a series of tectonic folds. Sediment flux from the fold-thrust belt reflects both tectonic growth of the fold structures but also the extent of exposure of resistant versus weak lithologies. For a landscape dominated by bedrock channels, the time required to reach equilibrium (90% of equilibrium sediment flux) with a given rate of tectonic uplift is proportional to the rock erodibility c_r , the rock uplift rate U , and the spatial scale (width) of the uplifting rock region L ,

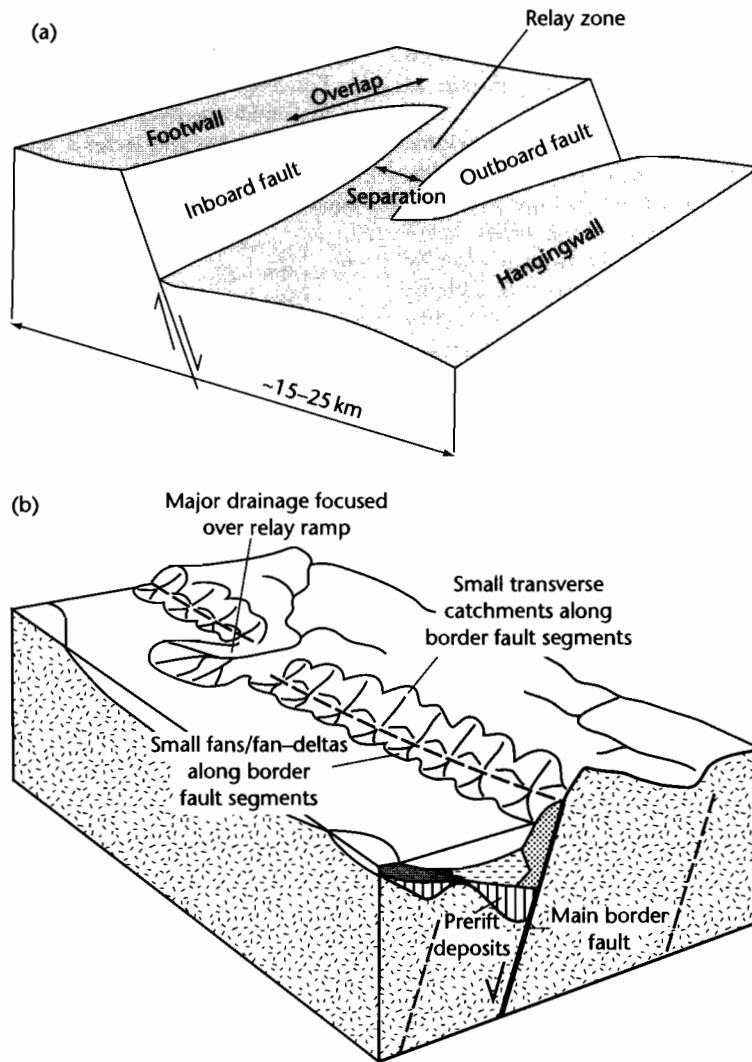


Fig. 7.29 (a) Perspective view of a soft-linked extensional relay zone; (b) Conventional view of relay zones as sites of large fan systems, whereas the main border faults have small transverse catchments and small fans/fan deltas.

$$\tau = k \frac{U^{\left(\frac{1}{n}-1\right)} L}{c_v^{1/n}} \quad (7.46)$$

where n is the exponent for slope in equation (7.35), commonly assumed to be $2/3$. Calibrated against model output from a landscape evolution model used to simulate the topography of the Zagros (using $c_v = 0.02$ to 0.2 m yr^{-1} , $L = 40 \text{ km}$, and $U = 1 \text{ mm yr}^{-1}$), the coefficient

of proportionality k in (7.47) is $7-10$. The geomorphic response time τ for sediment flux is between $c. 0.1 \text{ Myr}$ and 4 Myr for the weak and resistant lithologies respectively. For the resistant lithologies, the geomorphic response time is very long ($>1 \text{ Myr}$). In this case, it is most likely that periods of different thrust displacement rate in the fold-thrust belt would not be discernible in the stratigraphic record of neighboring foreland and thrust-sheet-top basins. However, small thrust-related anticlines

composed of weak lithologies should respond quickly to changes in tectonic boundary conditions, and produce a recognizable pulse of sediment in the basin. Figure 7.30 shows the evolution of sediment flux through time as rocks with different erodibility are unroofed.

It is apparent from a casual inspection of topographic maps that some streams cut transversely through folds, whereas others are deflected around their tips (Fig. 7.31). For example, in the Marche region of the Italian Apennines, a series of rivers drain to the Adriatic coast by cutting straight through the points of maximum tectonic uplift in NW–SE oriented folds (Alvarez 1999). The impact of growing tectonic structures on drainage patterns has been discussed by a number of authors (Jolley et al. 1990; Burbank and Vergés 1994; Talling et al. 1995;

Burbank et al. 1996; Gupta 1997). One of the major impacts for basin analysis is that sediment entry points into basins may be shifted by growing tectonic structures.

The simplest approach to understanding this problem is to consider a river that is in equilibrium between channel incision and tectonic uplift rates. For bedrock streams, we can modify equation (7.35) for the case of equilibrium to give

$$\frac{U}{c_v} = \left(\frac{Q_w}{Q_*} \right)^m S^n \quad (7.47)$$

If the uplift rate of rocks in the fold crest region is high ($U = 0.01 \text{ m yr}^{-1}$) and the stratigraphy is strongly resistant ($c_v = 0.025 \text{ m yr}^{-1}$), the dimensionless ratio U/c_v is high

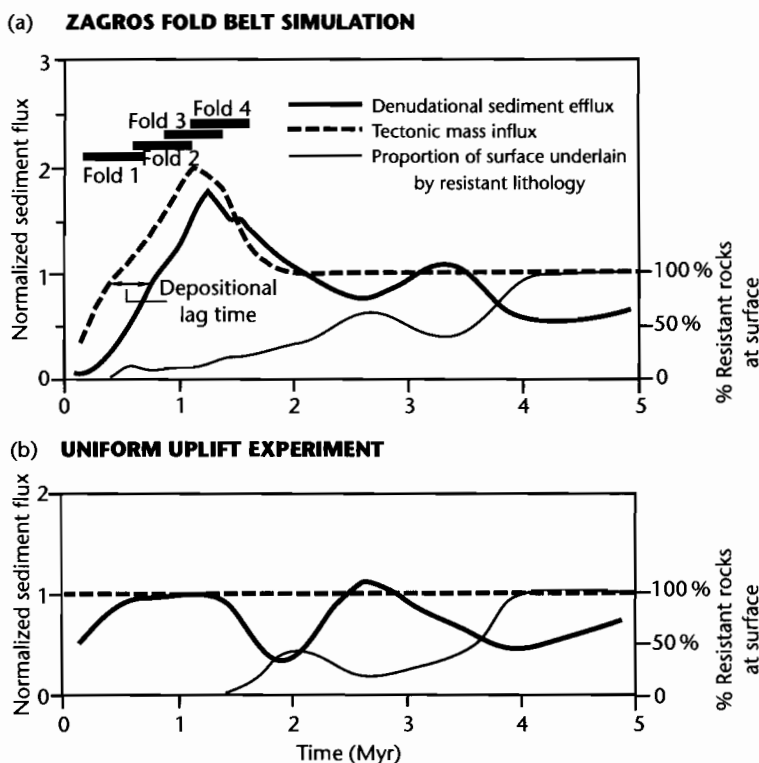


Fig. 7.30 Landscape evolution model results of the unroofing of folds in the Zagros fold-thrust belt. (a) Tectonic influx from uplift of rock (dashed line) and sediment efflux out of the model grid (solid line) versus time. In this simulation, four anticlinal folds grow progressively in time. Note the lag time between tectonic influx and depositional response of $<0.5 \text{ Myr}$ during the growth phase of the folds. The thin solid line shows the percentage of resistant rocks exposed at the land surface as a function of time. Note that the decrease then increase of sediment efflux is due to this variation in erodibility of outcropping rocks; (b) Sediment efflux in which the variations are solely due to lithological variations in the stratigraphy being unroofed. Tectonic influx is spatially and temporally uniform. After Tucker and Slingerland (1996). Reproduced courtesy of Blackwell Publishing Ltd.

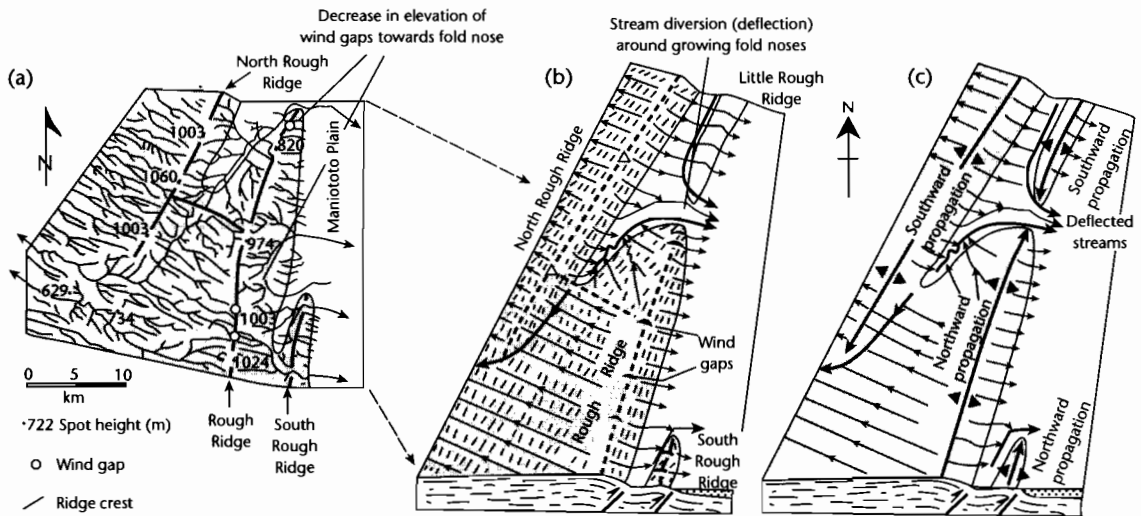


Fig. 7.31 Evolution of landscape in the face of growing folds, exemplified by the Southern Alps of central Otago, New Zealand (after Jackson et al. 1996). (a) Drainage network, fold crests, plunging fold noses, water gaps, wind gaps, and their elevations in the vicinity of Rough Ridge. Note the decrease in elevation of the wind gaps towards the fold nose; (b) Schematic diagram of drainage pattern, showing clear diversion of drainages around the nose of each growing fold; (c) Interpretation of fold propagation of same region of Rough Ridge and the resultant drainage development. Reproduced courtesy of Pergamon Press, Oxford.

(0.4), indicating that a stream is likely to be deflected. If, however, the uplift rate of rocks in the fold crest region is low ($U = 0.001 \text{ m yr}^{-1}$) and the rocks are weakly resistant to erosion ($c_r = 0.25 \text{ m yr}^{-1}$), U/c_r is low (0.004), indicating that the discharge-slope product of the stream may be sufficient to cut through the growing anticline. As a growing fold emerges, the width of the fold should increase. Field studies (e.g., Burbank et al. 1996; Jackson et al. 1996) suggest that if the elevation of the entrance and exit of the fold are fixed, the widening of the fold may cause a decrease in stream gradient and stream power, leading to defeat of the stream by the growing structure (see eqn 7.47). Alternatively, aggradation upstream of the entrance to the fold may cause avulsion of the stream to a lower position of the floodplain, effectively diverting the stream away from the growing fold. Deflected (defeated) streams are commonly captured by adjacent streams, which increases their discharge, allowing them to incise through the growing fold. The interaction of river drainage, erosion, topography and tectonic displacements is currently a rich area of research.

Coupled tectonic-erosion models at the scale of whole orogens, discussed in §4.6 and §4.7, involve the description of the tectonic deformation of the lithosphere in zones of convergence, coupled with a surface landscape of hillslopes and active channels and depositional basins (Beaumont et al. 1992, 1996b; Willett et al. 1993; Kooi and Beaumont 1994, 1996). As we have seen (§4.7), orogenic wedges with an asymmetry of climate (precipitation) on windward and leeward flanks are associated with an asymmetry of exhumation of deep crustal rocks. A structurally much simpler situation at a similar spatial and temporal scale is provided by the classic mega-escarpments found along segments of passive margins (Gilchrist and Summerfield 1990). The high escarpments of southern India (Western Ghats) (Gunnell 1998), Namibia-South Africa (Gallagher and Brown 1999), and SE Australia (Seidl et al. 1996) are good examples. Landscape evolution models of passive margin mega-escarpments are found in Kooi and Beaumont (1994) and Braun and Sambridge (1997).